

Sensitivities of Maritime Tropical Trimodal Convection to Aerosols and Boundary Layer Static Stability

G. ALEXANDER SOKOLOWSKY,^a SEAN W. FREEMAN,^a AND SUSAN C. VAN DEN HEEVER^a

^a *Department of Atmospheric Science, Colorado State University, Fort Collins, Colorado*

(Manuscript received 30 September 2021, in final form 18 March 2022)

ABSTRACT: A trimodal convective cloud distribution is commonly observed within the tropics due to the tropical-mean thermodynamic environment. The goal of this research has been to examine the integrated impacts of thermodynamic and aerosol properties on both the convective environment and the properties of the cloud modes themselves. This has been achieved by using LES experiments in which various thermodynamic and aerosol environments were independently and simultaneously perturbed. The key conclusions from this study are 1) large amounts of aerosol loading and low-level static stability suppress the bulk environment and the intensity and coverage of convective clouds; 2) cloud and environmental responses to aerosol loading tend to be stronger than those from static stability; 3) the effects of aerosol and stability perturbations modulate each other substantially; 4) the deepest convection and highest dynamical intensity occur at moderate aerosol loading, rather than at low or high loading; and 5) most of the strongest feedbacks due to aerosol and stability perturbations are seen in the boundary layer, though some are stronger above the freezing level. These results underscore the importance of considering the thermodynamic environment's impact on aerosol-induced convective invigoration while highlighting the dominance of aerosol impacts on the trimodal distribution and revealing synergies between thermodynamics and aerosols.

KEYWORDS: Aerosols; Clouds; Convective storms; Feedback; Glaciation; Radiative forcing; Storm environments; Thermodynamics; Cloud resolving models; Idealized models; Large eddy simulations; Numerical analysis/modeling

1. Introduction

Convective clouds are ubiquitous within the tropics and play important roles in energy and moisture transport on both local and global scales (Riehl and Malkus 1958; Malkus and Riehl 1964; Schumacher et al. 2004; Harrop and Hartmann 2015). These clouds follow a trimodal distribution of cumulus, cumulus congestus (hereafter “congestus”), and cumulonimbus clouds first recognized by Johnson et al. (1999), in contrast to older bimodal models of tropical convection focusing solely on cumulus and cumulonimbus (Schubert 1976; Randall 1980; Emanuel 1994). This trimodal distribution manifests due to the existence of three tropical-mean layers of elevated stability (Johnson et al. 1999). The individual modes also have a myriad of sensitivities to aerosol properties (Tao et al. 2012). Due to the connections between the modes and their environment, altering the bulk environment (mesoscale thermodynamic, condensate, and aerosol structure) may strongly impact the development of clouds within it, which subsequently also feeds back onto the environment.

Cumulus are the shallowest and most numerous convective clouds, both within the tropics and globally, and tend to be short-lived, dynamically weak, and lower in precipitation production versus their deeper counterparts (Johnson et al. 1999). These shallow tropical cumuli typically cease growing below the tropical-mean trade wind inversion around 2 km above ground level (e.g., Rauber et al. 2007; Ghate et al. 2016), and are “closely linked to turbulence within the marine boundary layer that is primarily driven by the surface turbulent

fluxes, radiative cooling, and wind shear” per Ghate et al. Not only are these clouds variable in nature and sensitive to marine boundary layer characteristics (Wood et al. 2011), but they also strongly contribute to the transport of heat and moisture within the boundary layer (Schumacher et al. 2004) and act as a “humidity throttle” on deep convection within the ITCZ core (Negggers et al. 2007).

Riehl and Malkus (1958) identified the role of cumulonimbus clouds, which they hypothesized to be undilute and referred to as “hot towers,” in surface-to-tropopause transport of heat and mass within the tropics. These clouds often extend to the tropopause, and based on the assumption of undilution, Riehl and Malkus determined that about 1500–5000 hot towers were required to support the heat losses and energy export from the tropics. Later theoretical and modeling studies (e.g., Zipser 2003) found this assumption to be unnecessary if boosts to moist static energy from glaciation were accounted for in balancing cloud entrainment. Tropical cumulonimbus may manifest as isolated convective towers, or as parts of larger cloud systems (Cotton et al. 2011). Isolated cumulonimbus heat through the troposphere, though organization and convective/stratiform percentage affect the heating profile structure (Schumacher et al. 2004).

Congestus clouds were only recognized as being an important part of the trimodal distribution with the seminal work of Johnson et al. (1999), despite having been identified over 100 years earlier (Maze 1889). Congestus are common in the tropics and exhibit a vertical extent reaching to the freezing stable layer (~4–6 km in the tropics; Johnson et al. 1999) and sometimes beyond (Luo et al. 2009). Johnson et al. found that congestus produced 28% of convective rainfall in the Tropical Ocean and Global Atmosphere Coupled

Corresponding author: G. Alexander Sokolowsky, g.alex.sokolowsky@colostate.edu

Ocean–Atmosphere Response Experiment (TOGA COARE; Webster and Lukas 1992) field campaign and suggested, as have others (Ruppert and Johnson 2015), that congestus clouds precondition the environment for deep convection. Some other studies (Hohenegger and Stevens 2013) found evidence for this hypothesis lacking in favor of mesoscale organization driving this preconditioning. Radiative–convective equilibrium (RCE) studies of trimodal convection conducted by Posselt et al. (2008) identified the formation of vertical circulations separated by the trade, freezing level, and tropopause inversions, the middle one of which is likely to impact upscale growth of congestus into deeper convection. Luo et al. (2009), for example, classified congestus into transient and terminal categories depending on their buoyancy at the freezing level. Congestus heating profiles resemble those of shallow cumulus and isolated cumulonimbus, but typically extend to the freezing layer (Schumacher et al. 2004, 2007).

Both the thermodynamic and aerosol environments in and around the Maritime Continent (MC), and the Philippines more specifically, are subject to a great deal of variance, which, as stated previously, influences cloud properties. These environments and associated interactions between aerosols, clouds, and thermodynamics were studied extensively during the recent Cloud, Aerosol, and Monsoon Processes Philippines Experiment (CAMP²Ex; Reid et al. 2022, manuscript submitted to *Bull. Amer. Meteor. Soc.*) field campaign conducted by NASA, NRL, and the Manila Observatory (MO). Thermodynamically, this region is well characterized by the tropical west Pacific warm pool environment identified by Yanai et al. (1973) but is also subject to natural variance including several large-scale oscillations that alter thermodynamic environments and influence cloud fields. The aforementioned Posselt et al. study identified that the three prominent tropical-mean stable layers separate vertical circulations, and thus variations in these layers (as well as any changes due to large-scale oscillations) can substantially impact the convection produced here (e.g., Del Genio and Kovari 2002; Masunaga et al. 2005; Jakob et al. 2005; Benedict and Randall 2007; Del Genio et al. 2012; Toms et al. 2020a,b).

Aerosol particles in the MC originate from a variety of sources: transportation, agriculture, heavy industry, biomass burning, and natural marine processes, among other causes, and number concentrations of these particles can range from tens to thousands per cubic centimeter (Reid et al. 2013, 2016a,b; Hilario et al. 2020). Aerosols directly scatter solar radiation (the “direct effect”; Charlson and Pilat 1969) and impact clouds via cloud–aerosol interactions or “aerosol indirect effects” (AIEs), which have also been observed in this geographic region (Rosenfeld and Lensky 1998). Increases in aerosol number concentrations have long been recognized to produce a narrower distribution of drops than would be in the presence of lower concentrations (Squires 1958), thereby resulting in a suppression of warm rain production (e.g., Squires and Twomey 1960; Warner and Twomey 1967), an increase in cloud albedo (e.g., Twomey 1974, 1977; Twomey et al. 1984) and lifetime (Albrecht 1989), and reduced precipitation in low clouds (e.g., Feingold et al. 1996; Xue et al. 2008; Saleeby et al. 2015). Deeper convective clouds have far more complex

AIEs that have been more challenging to disentangle. Many studies have discussed convective invigoration as an AIE in deeper convection (Andreae et al. 2004; Khain et al. 2005; van den Heever et al. 2006; Rosenfeld et al. 2008; Fan et al. 2009; Altaratz et al. 2010), though such findings of invigoration have been disputed (Grabowski 2018; Varble 2018) or have not been uniform with loading (Tao et al. 2012; Altaratz et al. 2014; Marinescu et al. 2021). Some of this uncertainty appears rooted in aerosol-induced convective invigoration being a balancing act between condensate loading, buoyancy, and updraft strength (e.g., Lebo and Seinfeld 2011; Lebo et al. 2012; Grabowski and Morrison 2020; Igel and van den Heever 2021) and the impacts to ice-phase processes, with some studies showing weaker updrafts for cold-based clouds (Igel and van den Heever 2021) or a mixed response across modeling platforms despite robust warm-phase invigoration (Marinescu et al. 2021). In contrast to the deep convective mode, relatively little attention has been paid to congestus. Li et al. (2013) and Sheffield et al. (2015) are among the few who have specifically explored aerosol impacts on congestus, and despite different modeling frameworks, both found a dynamical invigoration of congestus from increases in aerosol content.

The goal in this study is to use high-resolution numerical models to explore how individually and simultaneously varying initial low-level thermodynamic and aerosol properties affect the evolution of the bulk environment and the nature of the three modes of the tropical convective cloud distribution contained within it. To address this goal, we ran a suite of idealized LES model experiments for two full diurnal cycles in which we covaried the initial thermodynamic and aerosol environments. Section 2 describes our model and experimental setups; section 3 details our results and analysis with foci on the bulk environment and convective cloud modes; and section 4 presents our conclusions and future work directions.

2. Model setup and experiments

a. Model setup

The simulations were conducted using the Regional Atmospheric Modeling System (RAMS) v. 6.2.12 (Pielke et al. 1992; Cotton et al. 2003; Saleeby and van den Heever 2013; van den Heever et al. 2021). RAMS is a fully compressible, nonhydrostatic model with bin-emulating two-moment bulk microphysics (Meyers et al. 1997), 2-stream radiative transfer (Harrington 1997), a fully interactive land surface model (Lee 1992; Walko et al. 2000), and a sophisticated aerosol scheme that allows for radiative interactions (Saleeby and van den Heever 2013).

For this study, we chose to run RAMS as an LES model (Table 1) on a grid of 150 km × 150 km × 17.6 km. We used a horizontal grid spacing of 100 m, with vertical grid spacing stretched from 50 to 300 m, and a time step of 0.75 s with a total integration time of 48 h. The domain was centered at 4.46°N, 126.9°E (south of Mindanao in the Philippines) and the surface was fully ocean, with a uniform SST of 302.1 K (area averaged from 3.25° to 5.50°N and from 125.75° to 128.00°E in European Centre for Medium-Range Weather Forecasts reanalysis (ERA5) data (Hersbach et al. 2018).

TABLE 1. A summary of the RAMS LES model options and experimental configuration used in this study.

Model aspect	Setting
Model version	RAMS v. 6.2.12 (Pielke et al. 1992; Cotton et al. 2003; Saleeby and van den Heever 2013; van den Heever et al. 2021)
Dimensionality	3D
Grid	Arakawa C grid (Arakawa and Lamb 1977) Cartesian projection centered at 4.4673°N, 126.900°E $dx = dy = 100$ m 1500 × 1500 x - y grid points (150 km × 150 km domain) 98 stretched vertical levels dz stretched from 50 to 300 m at 1.026 ratio Model top ~ 17.6 km
Time step	0.75 s
Simulation duration	48 h, starting at 0000 UTC 21 Aug 2018
Boundary conditions	Cyclic in both horizontal directions Four Rayleigh damping layers at top beneath rigid lid Rigid bottom level with a fixed SST and no land surface
Surface treatment	LEAF-3 model (Lee 1992; Walko et al. 2000) Fully ocean domain with constant SST = 302.1 K Set from spatially averaged ERA5 data (Hersbach et al. 2018)
Initialization	Horizontally homogeneous initial sounding—averaged from a region producing mostly shallow convection in a basin-scale simulation nudged with ERA5 data (Freeman et al. 2019, 2022, manuscript submitted to <i>J. Atmos. Sci.</i>) Convection initialized with random perturbations
Microphysics	Two-moment bin-emulating bulk (Meyers et al. 1997) Cloud, drizzle, rain, pristine ice, snow, aggregates, graupel, hail species Ice nucleation following DeMott et al. (2010)
Aerosol treatment	Overall treatment follows Saleeby and van den Heever (2013) Initialized as exponential profile based on prescribed surface concentration Ammonium sulfate CCN aerosol; no giant CCN (GCCN), dust, or sea salt Composite ice nuclei (IN; DeMott et al. 2010) with surface concentration 10 L^{-1} No aerosol sources or sinks, aerosol radiative activity on
Radiation	Harrington 2-stream radiation (Harrington 1997) Updated every 5 min

As these experiments are idealized, small islands present in reality were removed from our domain for simplicity. The top boundary was a rigid lid, with four Rayleigh damping levels for dispersion of gravity waves, and the lateral boundaries were cyclic. Aerosols were configured to be solely ammonium sulfate, a common species in the MC (Atwood et al. 2017), with a lognormal distribution that had a geometric mean radius of $0.09 \mu\text{m}$ and geometric standard deviation of 1.8 (J. Reid and J. Wang 2020, personal communication). No sources or sinks of aerosols were included but they were radiatively active and could advect and diffuse around the domain. The basic initial thermodynamic profile is horizontally homogeneous (Fig. 1a), and was produced by interpolating a coarser basin-scale simulation by one of the authors (Freeman et al. 2019, 2022, manuscript submitted to *J. Atmos. Sci.*) onto a finer grid, and then area averaging the thermodynamics from 4.2° to 4.6°N and from 127.2° to

128.8°E on 21 August 2018, a region which primarily contained shallow convection. Over the course of the model runs, all experiments described below produce convection at a range of depths, accurately capturing the trimodal distribution (Fig. 2).

b. Experiment setup

In our numerical experiments, we initialized the simulations with three different thermodynamic profiles and three different surface aerosol concentrations, comprising a total of nine experiments (Table 2). The naming scheme we use for reference, also shown in Table 2, combines a stability prefix (“ls,” “ms,” or “hs” for low, medium, or high stability, respectively) with an aerosol suffix (“100,” “500,” or “3000,” denoting the surface aerosol mixing ratio in mg^{-1}). The thermodynamics shown in Fig. 1a were used for the ms runs, and the ls and hs profiles were perturbed by applying a negative or positive

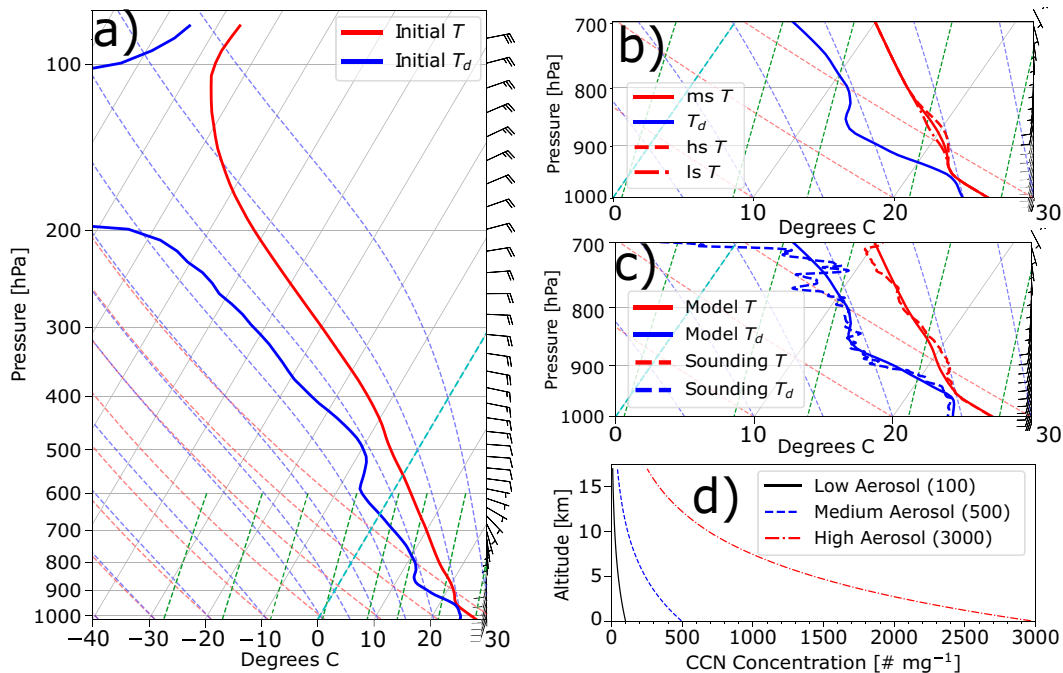


FIG. 1. Thermodynamic and aerosol profiles used in our LES numerical experiments. Various thermodynamic and aerosol profiles are shown demonstrating the range of thermodynamic and aerosol conditions applied: (a) the medium-stability thermodynamic profile derived from the Freeman et al. (2019) basin-scale run, (b) the temperature perturbations applied, (c) a comparison of the domain-mean profile in the lower troposphere after 4 h of model time in the ms-100 simulation to a CAMP²Ex dropsonde observation from 1 Oct 2019, and (d) a depiction of the three initial aerosol profiles used.

Gaussian temperature perturbation, respectively, with a maximum amplitude of 0.5 K between ~600 and 2000 m above ground level (Fig. 1b). The Gaussian perturbation allows for a smooth perturbation of temperature without producing discontinuities in the thermodynamic profile, and these perturbations are representative of the static stability range seen in five CAMP²Ex flights (Reid et al. 2022, manuscript submitted to *Bull. Amer. Meteor. Soc.*) where similar cloud fields exhibiting convective clouds with a low cloud fraction were observed (Fig. 3). The ms-100 profile produces a simulation environment representative of CAMP²Ex and the west Pacific warm pool (Fig. 1c), and the details of the evolution of static stability is discussed in section 3. Aerosol profiles decay exponentially with height (initial setups seen in Fig. 1d), and the surface values used were based on observations made in the region of the field campaign (Reid et al. 2013, 2016a,b; Atwood et al. 2017; J. Reid and J. Wang 2020, personal communication). Aerosol advection and diffusion near the surface reduce our initial surface mixing ratio by about 15% at the end of the ls-100 simulation, and advection leads to some vertical stratification of aerosol, but the initial profile remains largely intact above the well-mixed surface layer. In our results and analysis, the ls-100 simulation was designated as our control simulation due to having the least stability and aerosol versus the remainder.

After conducting these experiments, our methodology for analyzing results largely seeks to capture the changes and responses in domain-wide and domain-mean cloud and

environmental qualities, and to further assess changes in certain key variables within the specific modes of the tropical trimodal convective distribution. Most of these properties were assessed at 5-min temporal resolution, though some of the analyses include temporally integrated contoured-frequency-by-altitude diagrams (CFADs; Yuter and Houze 1995), and spatiotemporal means of cloud properties. For all analyses, the first 2 h of simulation time were considered as model spinup and discarded. At each analysis time step, the total condensate field was masked to hide values less than 0.01 g kg^{-1} (the same threshold as van den Heever et al. 2011; Sheffield et al. 2015), and the “label” function from the Python SciPy package (Weaver 1985; Virtanen et al. 2020) was used to identify contiguous 3D regions of condensate above this threshold. All convective cloud regions were required to be contiguous in 3D space and have a cloud base below 2 km, with cumulus terminating below 4 km, congestus from 4 to 7 km, and deep convection above 7 km (Johnson et al. 1999; Sheffield et al. 2015; see examples in Fig. 2). The coordinates of different clouds were grouped by mode for our analysis, and below we report the means and standard deviations of key properties when at least one cloud of that mode was present. Our horizontal grid spacing of 100 m allows us to capture all modes of the tropical trimodal distribution, and is comparable to previous LES studies of cumulus clouds (e.g., Xue et al. 2008). However, the very smallest cumulus clouds (length of order ~200 m or less; Wang et al. 2009; Ghate et al. 2016) will not be adequately represented (Heus and

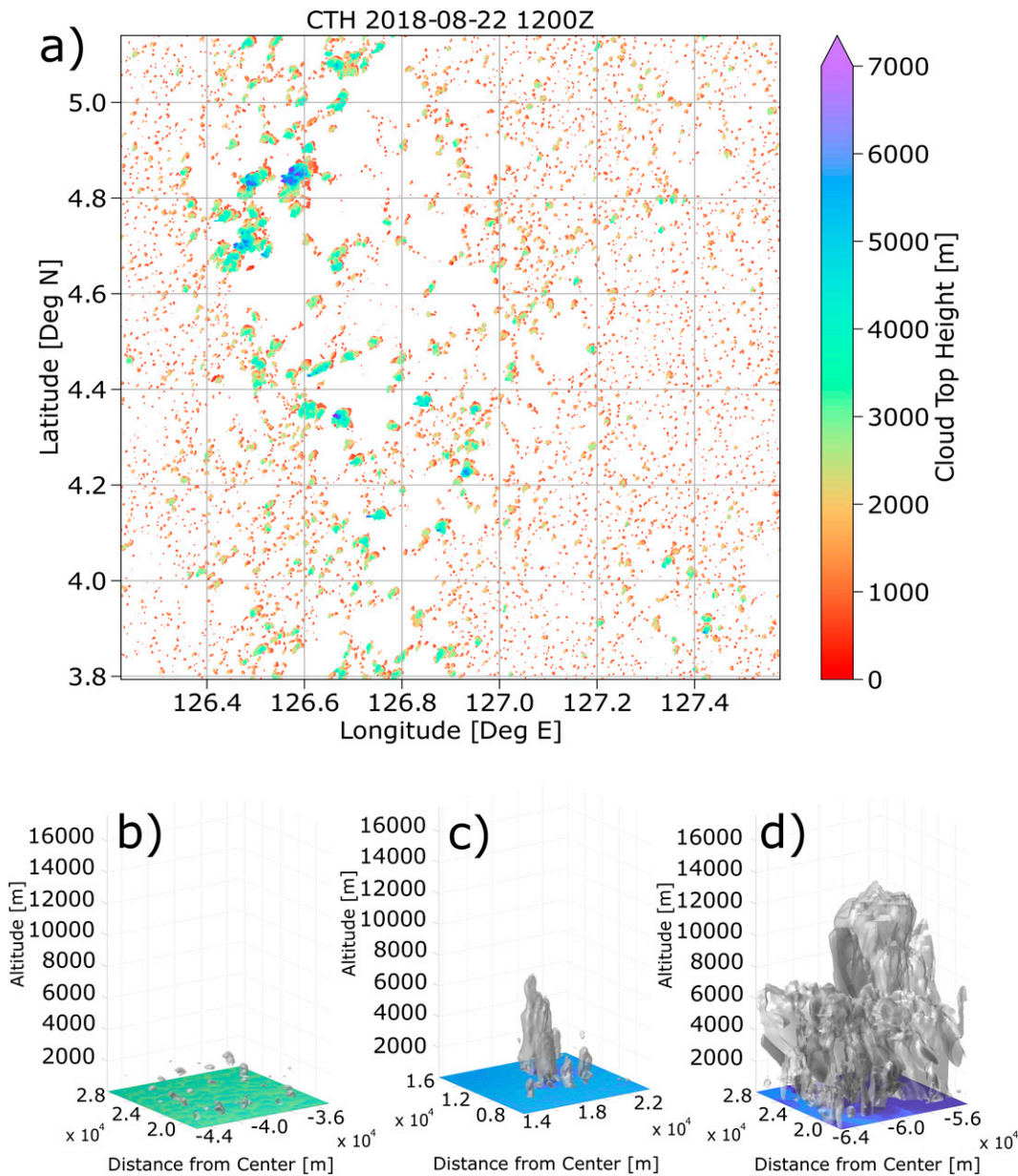


FIG. 2. Depictions of the cloud fields represented in the simulations. (a) A plan view of the cloud-top height field for the full domain of the ms-100 simulation after 36 h of model time; (b)–(d) examples of cumulus, congestus, and cumulonimbus, respectively, plotted on limited domains from different times in the ms-100 simulation.

Seifert 2013). As the vast majority of clouds (>90%) by surface area and volume are properly resolved, we feel that this grid spacing is sufficient for this study.

3. Results and analysis

a. Bulk dynamics and microphysics responses to static stability and aerosol

We start by providing an overview of the environmental evolution of our simulations, quantified via static stability, radiative transfer, cloud fraction, dynamical intensity (updraft

and downdraft strengths), and condensate glaciation. While Figs. 4g, 5g, 6g, 7g, 8g, 9g, and 10g represent the control simulation and show actual values of the property of interest, the remaining panels demonstrate differences or percentage changes from control (control being the ls-100 run; EXPERIMENT – CONTROL). Initial static stability and aerosol increase when moving upward and rightward among the figure panels, respectively. Precipitation responses largely reflected the findings of previous literature: with increased aerosol loading, the total precipitation and number of raining columns were reduced, while some of the raining columns did demonstrate increases in

TABLE 2. A depiction of the experimental suite presented within this study and the naming convention used. “B-V freq.” here denotes the Brunt–Väisälä frequency at initialization.

	Low aerosol (100 mg ⁻¹ at surface)	Medium aerosol (500 mg ⁻¹ at surface)	High aerosol (3000 mg ⁻¹ at surface)
High stability ~+6% max B-V freq. from Fig. 1a ~+0.85% mean B-V freq. from Fig. 1a	hs-100	hs-500	hs-3000
Medium stability Uses Fig. 1a profile	ms-100	ms-500	ms-3000
Low stability ~-6% max B-V freq. from Fig. 1a ~-0.85% mean B-V freq. from Fig. 1a	ls-100 (CONTROL)	ls-500	ls-3000

precipitation intensity (e.g., Albrecht 1989; Xue et al. 2008; Lebo and Seinfeld 2011; van den Heever et al. 2011; Tao et al. 2012; Saleeby et al. 2015). As these findings are not overly novel, they will not be discussed further in this study.

First, we examine the changes in environmental static stability. The Gaussian temperature perturbation for the ls-100 run produces a Brunt–Väisälä frequency profile with two low-level maxima at initialization, the stronger at ~700 m (coinciding

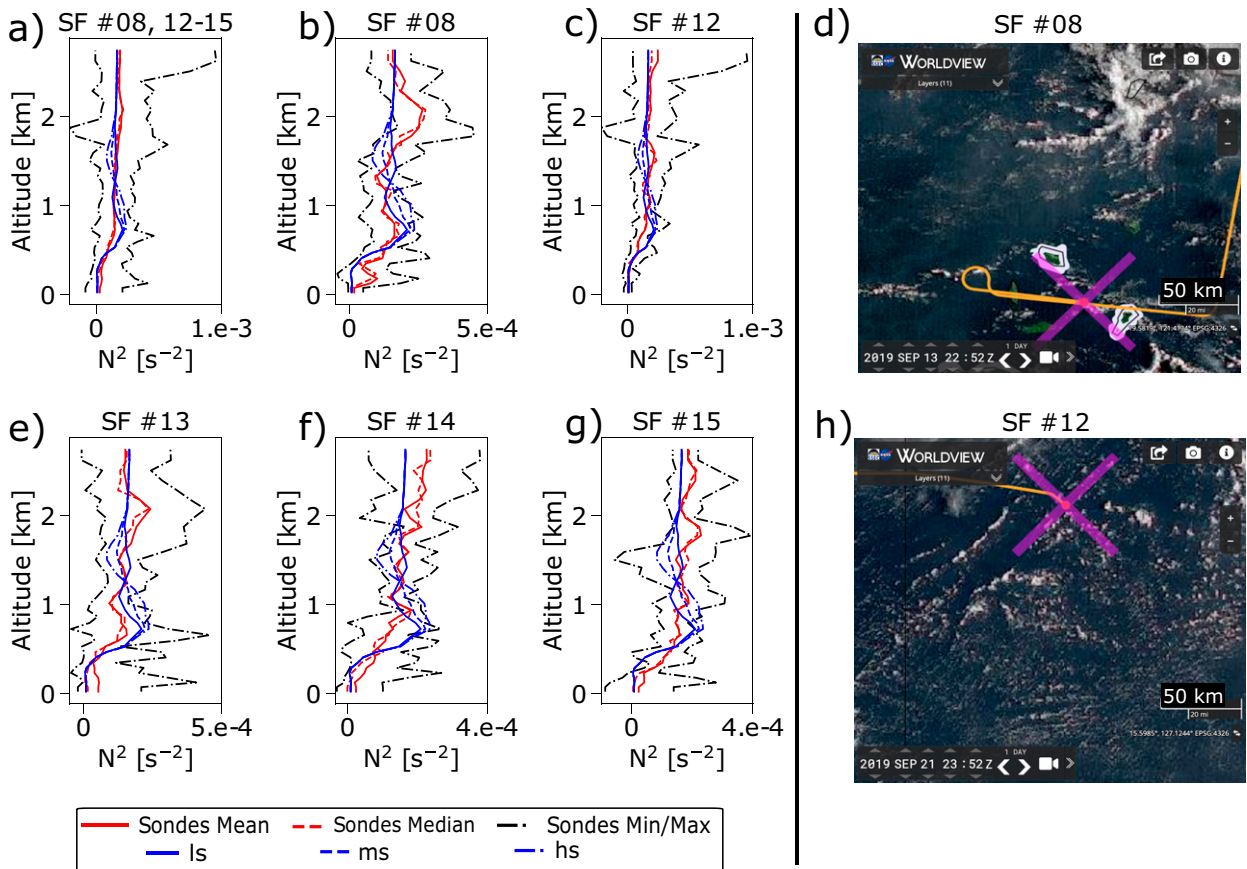


FIG. 3. Vertical profiles of our initial static stability settings (quantified as N^2 , the square of the Brunt–Väisälä frequency) vs those collected from CAMP²Ex dropsondes launched in conditions comparable to our simulations. (a) Values from all of science flights 8 and 12–15. (b),(c),(e)–(g) Values from the individual flights 8, 12, 13, 14, and 15, respectively. (d),(h) *Himawari-8* 1 km visible satellite imagery from science flights 8 and 12, respectively. The red solid and red dashed lines on the stability panels represent the sondes’ mean and median for each flight grouping, the black dash–dotted lines represent the sondes’ minimum and maximum for each grouping, and the solid, dashed, and dash–dotted blue lines represent the values from our low-stability, medium-stability, and high-stability simulation initial settings, respectively. Also note the different x -axis scaling between different panels. (d),(h) *Himawari-8* 1 km visible satellite imagery from science flights 8 and 12, respectively. In (d) and (h), P-3 position and flight track are denoted by the magenta \times symbol and orange line, respectively. [University of Wisconsin/NASA GeoWorldview website (<http://geoworldview.ssec.wisc.edu>)].

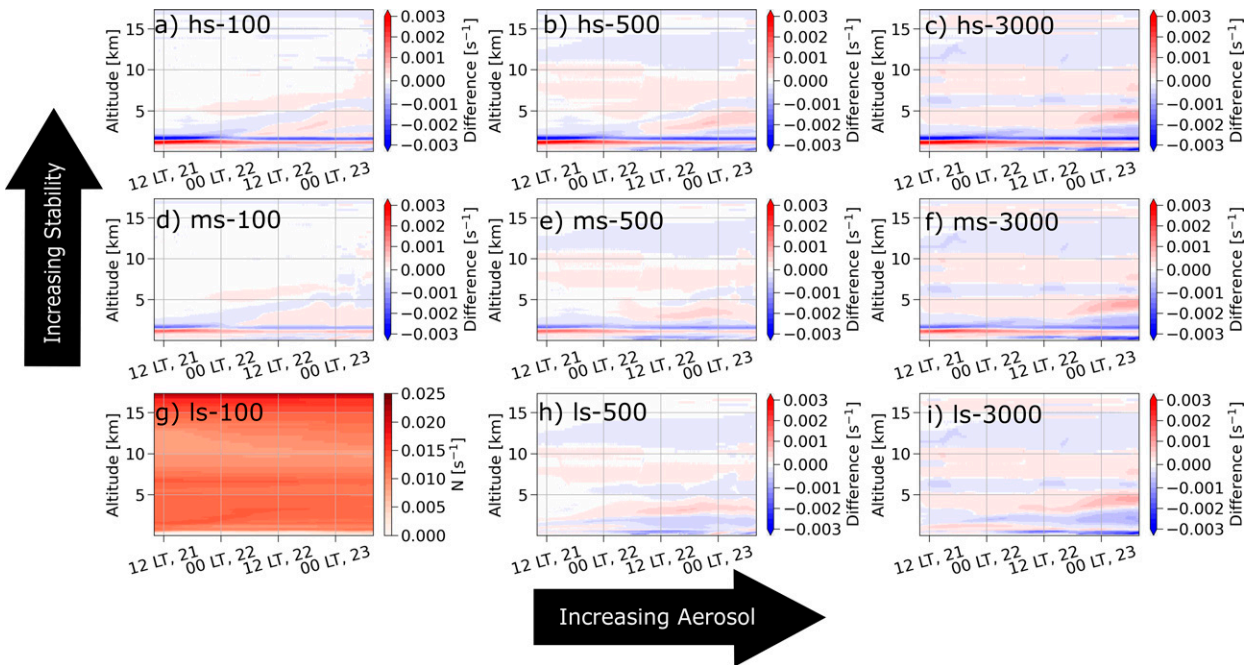


FIG. 4. Time–height series plots of (g) static stability (quantified as N , the Brunt–Väisälä frequency) for the control ls-100 simulation and (a)–(f),(h),(i) differences in total cloud fraction of the aerosol and static stability sensitivity experiments from the control ls-100 simulation. Differences from control less than $\pm 0.0001 \text{ s}^{-1}$ are indicated in white in (a)–(f), (h), and (i). Aerosol concentrations increase from left to right, and static stability increases from the bottom row to the top row as indicated by the solid black arrows.

with the stability peaks in our ms and hs runs) and the weaker around 1400 m, with the ms and hs runs exhibiting a single maximum at 700 m (Fig. 3). Two hours after initialization, a weak unstable surface layer develops due to our initial air–sea

temperature difference of about 1 K (similar to that seen in the basin-scale run) that, while persistent, does not robustly grow in either depth or strength (Fig. 4g). Qualitatively, the vertical locations of our initially perturbed stability maxima

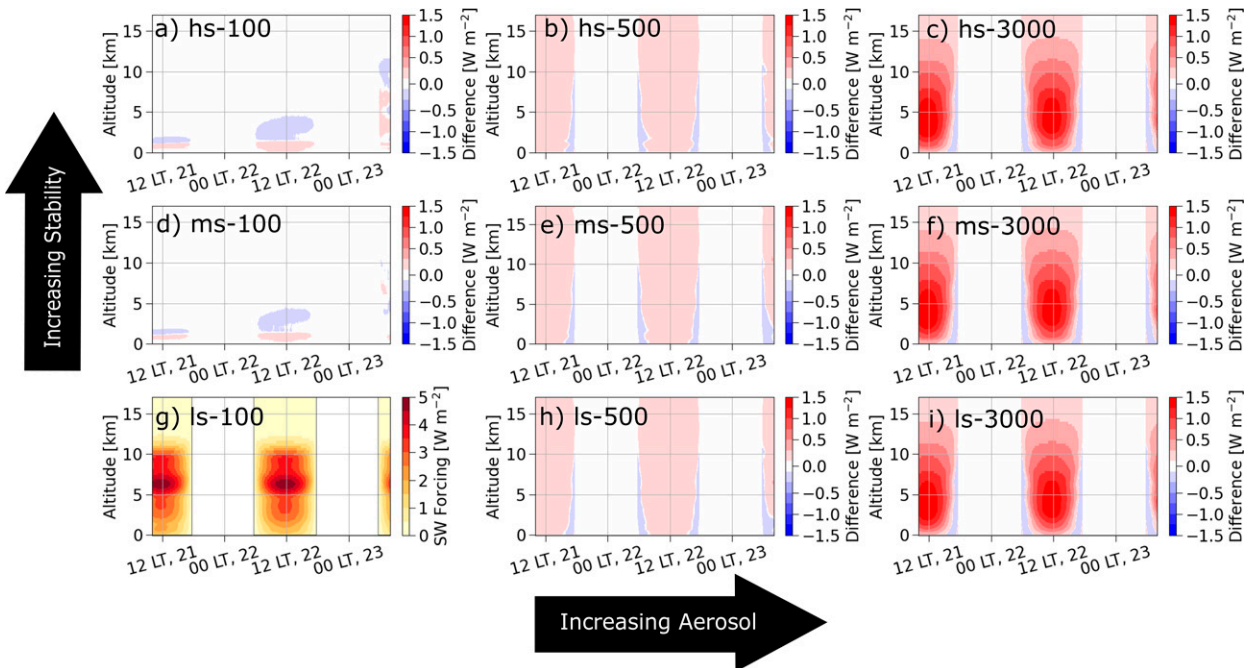


FIG. 5. As in Fig. 4, but for shortwave (SW) radiative forcing. Differences from control less than $\pm 0.01 \text{ W m}^{-2}$ are indicated in white in (a)–(f), (h), and (i).

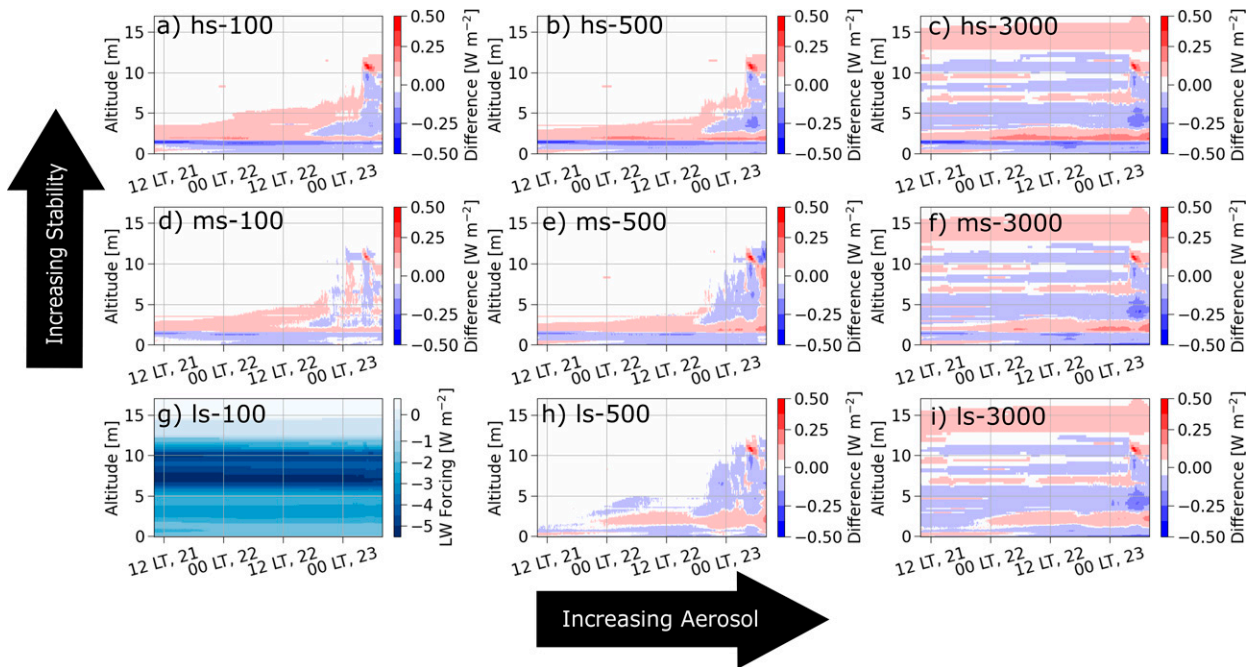


FIG. 6. As in Figs. 4 and 5, but for longwave (LW) radiative forcing. Differences from control less than $\pm 0.01 \text{ W m}^{-2}$ are indicated in white in (a)–(f), (h), and (i).

and minima narrow but otherwise vary little over the simulation, and the boundary layer gradually destabilizes in time (more so close to the surface) due to clear-sky nocturnal longwave (LW) cooling driven by our moisture profile in conjunction

with our fixed SST (Fig. 5). Due to low cloud fraction (which is in keeping with the CAMP²Ex observations, e.g., Figs. 3d,h), this clear-sky LW cooling, driven by the moisture profile, dominates the domain-wide LW signal. As the temporal frequency of

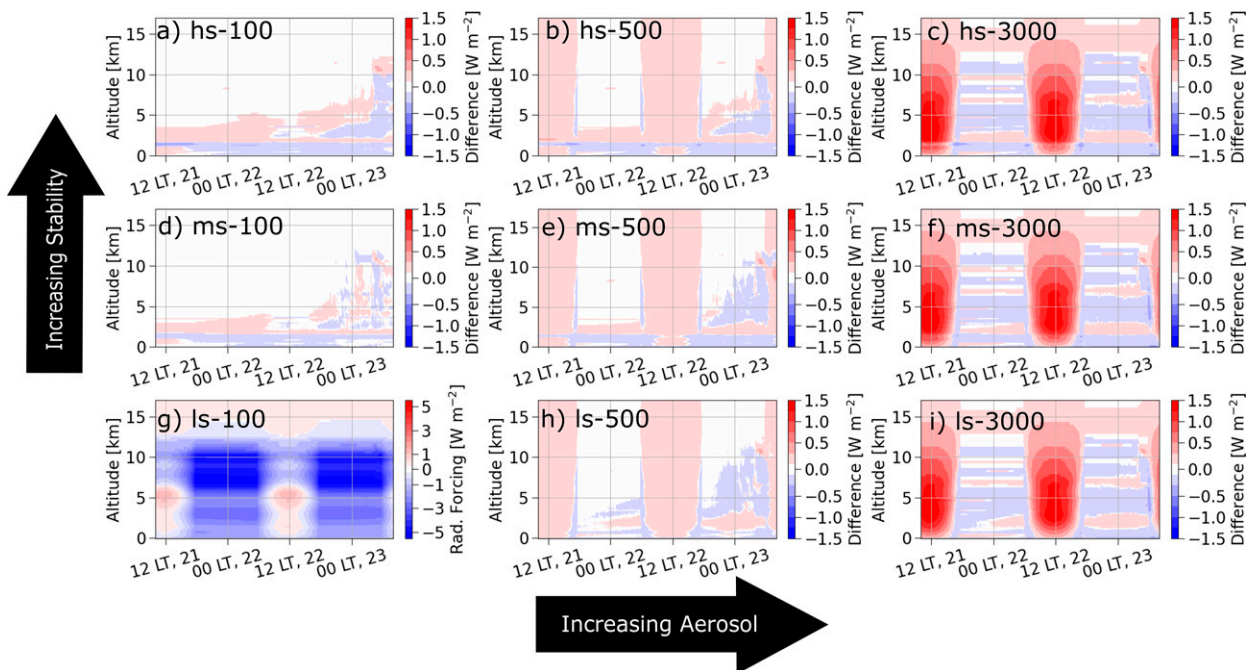


FIG. 7. As in Figs. 4–6, but for total radiative forcing. Differences from control less than $\pm 0.01 \text{ W m}^{-2}$ are indicated in white in (a)–(f), (h), and (i).

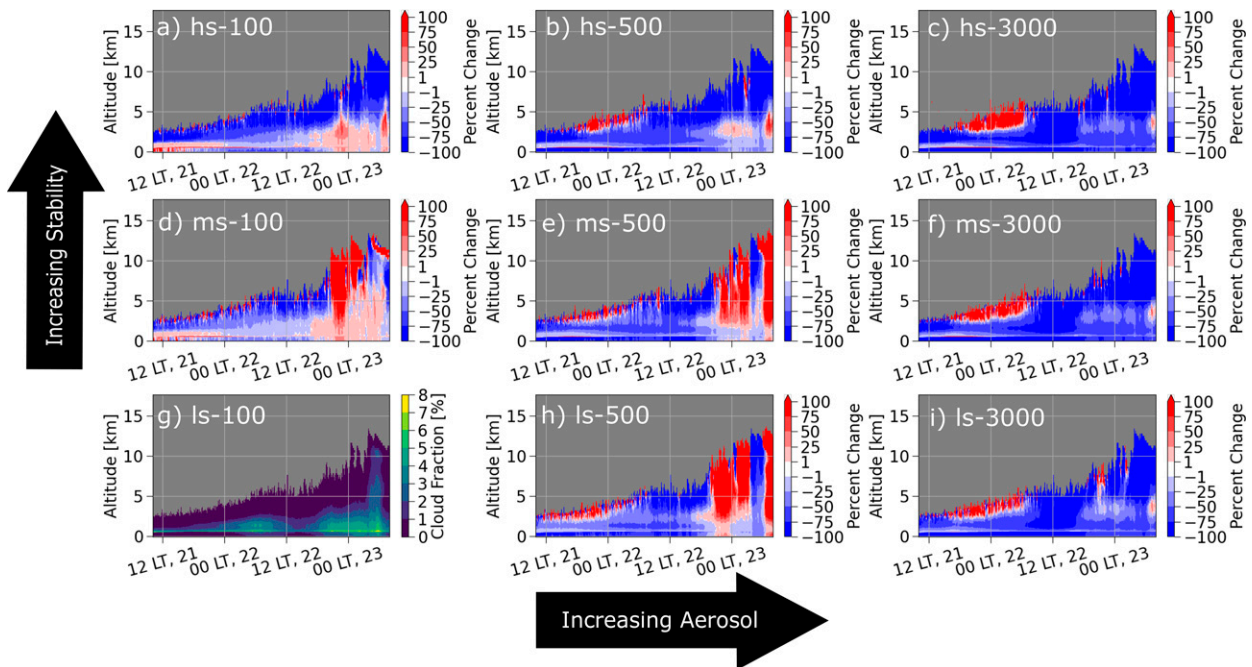


FIG. 8. As in Figs. 4–7, but for cloud fraction. Note that unlike Figs. 4–7, the difference plots show percentage changes rather than the actual difference in values. Time–altitude pairings where either (g) one or (a)(f),(h),(i) both simulations had a cloud fraction of zero were masked in gray. Percentage changes with a magnitude less than 1% are marked in white.

radiation updates (5 min) is coarser than our dynamical time step (0.75 s) and the cloud fraction is low (Figs. 2 and 8g), cloud impacts on radiative transfer beyond their bulk moisture transport are relatively small and uncertain versus the clear-sky changes. The contrast in update frequency may also impact changes in cloud cover and precipitation, as has been identified in previous studies (e.g., Matsui et al. 2018).

Aerosols also impact the stability evolution of the environment via changes to clear-air radiative transfer. The slight vertical stratification of aerosol has little effect on stability for the low- and midaerosol runs (Fig. 4, left and center columns), but leads to stability stratification at high aerosol (Fig. 4, right column). Though multiple scattering in the vertical is seen to enhance daytime shortwave (SW) heating (Figs. 6 and 7, center and right columns), this affects stability little in comparison to the changes in the LW profile from absorption by ammonium sulfate (Figs. 5 and 7). In this version of RAMS, these aerosols were comprised of an ammonium sulfate coating over a dust core, with a 10%–90% composition split, respectively, leading to greater absorption by our aerosols than pure ammonium sulfate. Stability and AIE impacts on clouds (discussed more in the following section) and ensuing changes in moisture transport also feed back on stability in the lower troposphere, though these are weaker than the initial stability perturbations (Figs. 3 and 4).

We now examine the simulation evolution in terms of cloud fraction (Fig. 8). Shallow boundary layer clouds are ubiquitous throughout the control simulation, but cover little area (ls-100; Fig. 8g). Thus, cloud coverage at any altitude remains low overall as is seen in some of the CAMP²Ex observations,

rarely exceeding 5% anywhere within the domain (Figs. 2, 3d,h, 8g). Clouds remain shallow until the first overnight period (~1735 LT 21 August–0540 LT 22 August), deepening overnight due to progressive moistening of the lower troposphere by boundary layer cumulus. The first congestus are produced around 0000 LT 22 August, and a deep convective cloud briefly appears about 12 h later. However, due to the low frequency of deep convection, cumulus clouds dominate the scene until the second sunset (~1735 LT 22 August). At 1800 LT 22 August, cumulonimbi with CTHs of 8 km emerge again, and subsequently deepen to 10 km at 0000 LT 23 August and 12 km at 0300 LT. In the final hours on the morning of the third day, deep convection decays, with maximum CTH reducing from over 12.5 km before sunrise to 11 km at the simulation's end (0800 LT 23 August).

Changes in static stability manifest the most strongly at low and moderate aerosol concentrations (Fig. 8, left and center columns), with the influence of stability becoming more muted as aerosol concentrations are increased (Fig. 8, right column). Moderate static stability (Figs. 8d,e) appears to favor deeper cloud penetration when compared with the control ls-100 run, though boundary layer cloud cover is slightly reduced. However, high stability (the top row of Fig. 8) generally suppresses cloud coverage. This behavior is consistent with previous studies: the trade wind stable layer is often not a true inversion in the deep tropics (Ghate et al. 2016), but the stronger it is, the more it inhibits cloud growth (Malkus 1958; Malkus and Riehl 1964; Johnson et al. 1999). Overall, increasing the static stability traps more moisture in the boundary layer, which is favorable for the development of

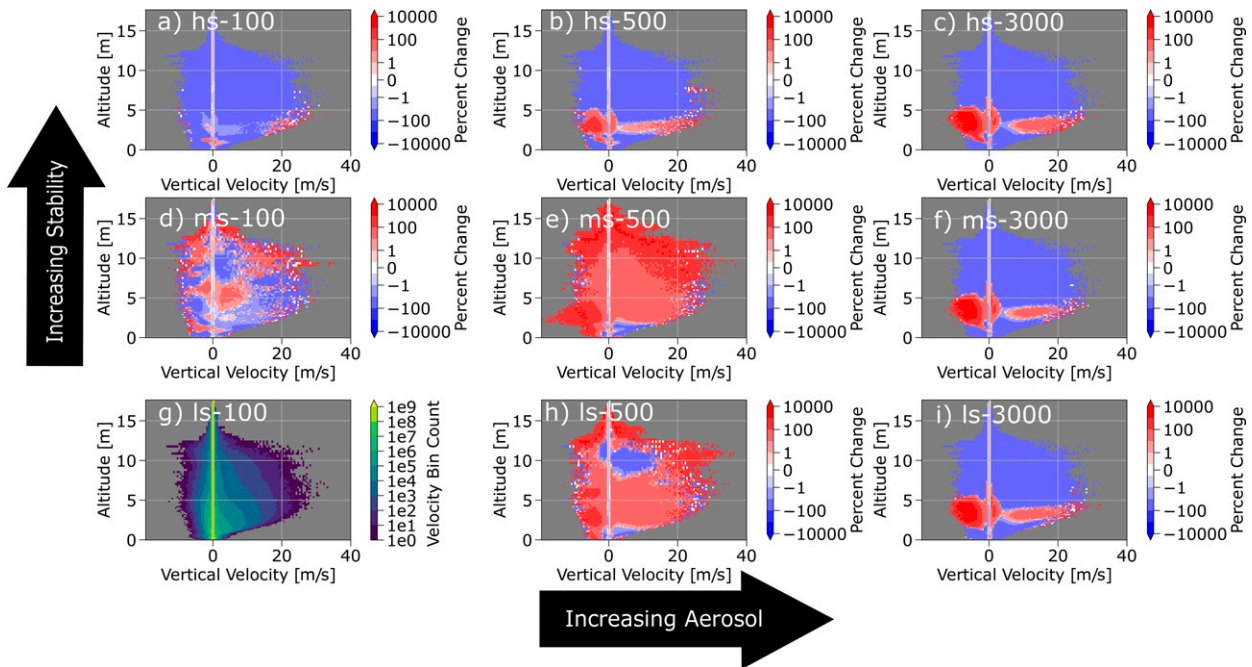


FIG. 9. CFAD diagrams of vertical velocity calculated using the entire domain and over all analysis times, for (g) the control ls-100 simulation and (a)–(f), (h), (i) percentage changes in bin count from the ls-100 simulation. Regions where either (g) one or (a)–(f), (h), (i) both simulations had a CFAD bin count of zero were masked in gray, and percentage changes less than $\pm 0.1\%$ are indicated in white in (a)–(f), (h), and (i). Aerosol concentrations increase from left to right, and static stability increases from the bottom row to the top row as indicated by the solid black arrows. Note that the color bars here are logarithmically scaled.

deep convection later, but too high an initial stability ultimately impedes this convective development due to the greater buoyancy required to break through the stable layer.

Responses to increased aerosol loading are similar to those for increased stability in the lower troposphere (Fig. 8, center and right columns). These responses arise due to two processes: 1) enhancement of the stability above the boundary layer by aerosol LW absorption; and 2) dynamic–thermodynamic–microphysical AIEs such as warm rain suppression (e.g., Albrecht 1989; Saleeby et al. 2015). Moderate aerosol loading leads to some enhanced production of deep convection, a finding seen in previous studies (e.g., Khain et al. 2005; Rosenfeld et al. 2008; van den Heever et al. 2011). However, the highest amount of aerosol loading does produce consistent trends of reduced cloud cover, likely due to increased entrainment and evaporation of the smaller cloud droplets produced from greater aerosol concentrations. This indicates a reduced sensitivity to changes in static stability for high aerosol loading.

Dynamical intensity, quantified by updraft and downdraft velocities domain-wide throughout the simulation (Fig. 9g, note the logarithmic scale) exhibits a broad range in strengths, although most vertical velocities are weak—an expected result considering that cloud fractions are low and the CFADs include both clear and cloudy regions. The frequency of updrafts and downdrafts tends to decrease in both directions the further they are from 0 m s^{-1} , with most falling between about -10 and 30 m s^{-1} . The distribution width also varies

little throughout much of the profile, though narrowing occurs above 12 km (a height that few clouds penetrate) and within the boundary layer (where static stabilities are the highest). Similar responses to cloud fraction for enhanced stability and aerosol are seen in the dynamical intensity: moderate aerosol increases result in increased dynamical intensity (Table 3, Figs. 9d,e,h), with strong enhancements in either stability or aerosol suppressing it (Table 3, Fig. 9, top row and right column). The only exception is for low-level vertical velocities, which are enhanced at high aerosol loading due to warm-phase invigoration. These changes, which are discretized by simulation initial characteristics, tropospheric altitude, and strength of vertical motion in Table 3, are reflective of the changes seen in cloud fraction, further illustrating the connections between vertical circulations and cloud field characteristics.

Finally, the relative contribution of ice to the total condensate illuminates some stark changes over the course of the simulation (Fig. 10g). As the 0°C level is located at $\sim 4.5\text{--}5$ km in each simulation, the vast majority of condensate below this altitude is liquid. Ice first emerges in the domain around 0600 LT 22 August, when some congestus clouds glaciate. As the congestus are primarily liquid, the ice ratios generally remain low until deep convective clouds become more frequent around 12 h later. After 1800 LT 22 August, we see a mixed-phase region from roughly 4.5–6 km, near-total glaciation above 9 km, and pulses of elevated and reduced ice ratios above and below the freezing level. These regions of greater and lesser ice ratios in the mixed-phase region indicate falling

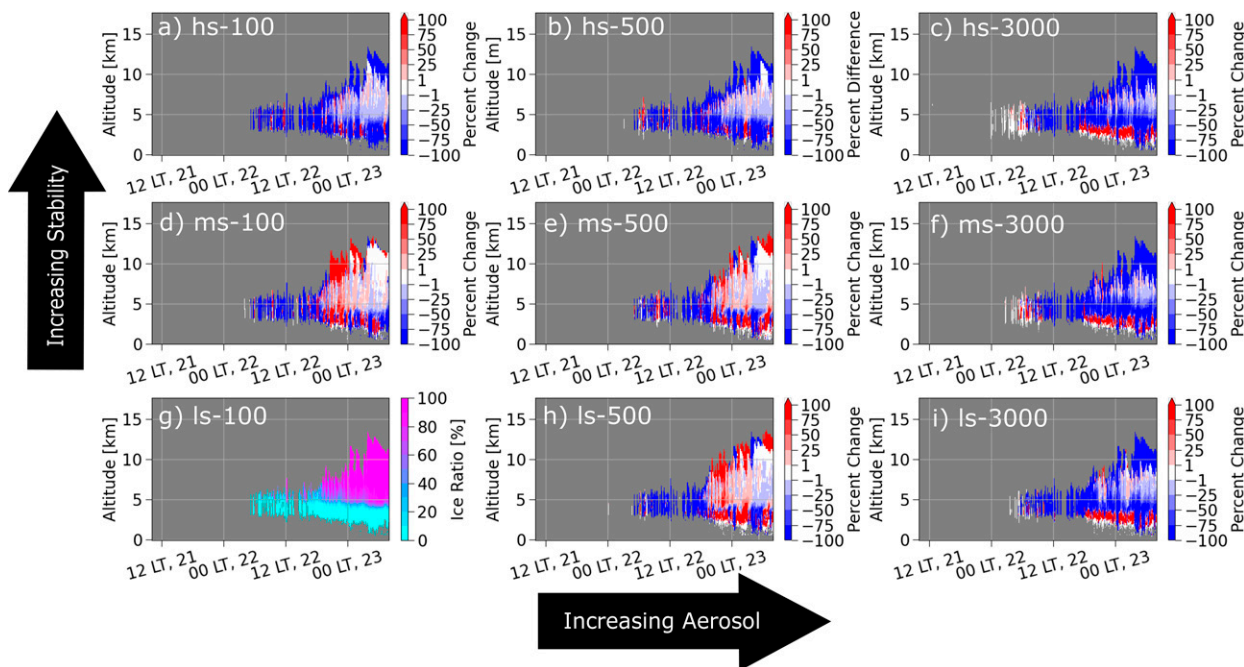


FIG. 10. As in Fig. 8, but for ice ratio (mean ice condensate mixing ratio/mean total condensate mixing ratio for each vertical level and time). For the difference plots, regions where the mean condensate mixing ratio was less than 0.01 g kg^{-1} were masked, areas where the control had no cloud were provided with the ice ratio of the simulation being compared, and percentage changes less than $\pm 1\%$ were indicated in white in (a)–(f), (h), and (i).

ice precipitation and lofted supercooled water, respectively. Ice-phase responses to enhancements in static stability and aerosol further reinforce and explain the changes seen in cloud fraction and dynamical intensity. At moderate stability and aerosol loading, we see a delayed onset of glaciation but later increases in both deep glaciated clouds and subfreezing level ice precipitation (Figs. 10d,e,h), indicating the importance of glaciation and the timing of these ice processes for cold-phase invigoration of deep convection. As previously discussed, high static stability impedes the vertical growth of shallower convection, which subsequently suppresses glaciation. Additionally, while moderate amounts of aerosol induce both warm- and cold-phase invigoration, high aerosol loading only produces the former, resulting in lower cloud tops, cloud coverage, and glaciation. This robust warm-phase invigoration, and more mixed response in the cold phase with suppression at the highest aerosol loading, are in agreement with the findings of recent studies of deep convection (Igel and van den Heever 2021; Marinescu et al. 2021; Park and van den Heever 2022).

Generally, our simulations initiate as a shallow cumulus field that gradually deepens and dynamically intensifies as diurnal cycles of convection and radiation progressively moisten the lower troposphere and destabilize the middle and upper troposphere. The initiation of deeper convection further impacts the evolution of the domain by deepening the vertical transport of moisture and producing considerably more precipitation, although cloud cover remains low overall. Since our idealized simulations lack the presence of SST variations,

SST feedbacks and large-scale wind disturbances that some studies have identified to be important to the diurnal cycle (e.g., Weller and Anderson 1996; Sui et al. 1997), some of this variability cannot be fully captured. However, the overall diurnal cycle and our understanding of the role of convective moistening are reasonably consistent with previous studies using a fixed SST (e.g., Liu and Moncrieff 1998). Increasing the static stability and aerosol both impact the thermodynamic evolution of the scene, with moderate (strong) enhancements in either of the two amplifying (suppressing) convective favorability. Last, it appears that impacts from changing both stability and aerosol may operate synergistically to invigorate convection (a “Goldilocks zone”) in some circumstances. This is most evident in the ms-500 simulation, which exhibits deeper convection, more widespread updraft and downdraft invigoration, and more vertically contiguous fluctuations of enhanced and reduced ice ratio (i.e., more lofting of supercooled water and precipitation of ice) than the control run. Stability-induced enhancement of boundary layer moisture coupled with greater condensational growth due to higher aerosol concentrations is a prime driver of this response.

Having examined these responses to aerosol and static stability, we now turn our attention to examining the response of each convective mode to these initial conditions. While shallow convection can and does grow upscale to deep convection in our simulations, considering each mode and its responses to aerosol and stability in relative isolation is important for understanding the role each mode plays in the evolution of

TABLE 3. A discretization of percentage changes in vertical velocities from the control simulation (ls-100) for the other eight model runs, categorized by vertical location, simulation initial characteristics, and strengths of updrafts and downdrafts. Low levels range from 0 to 4 km (corresponding to the possible CTH range of the cumulus mode), midlevels from 4 to 7 km (corresponding to the CTH range of the congestus mode), and upper levels from 7 km up (corresponding to the CTH range of the cumulonimbus mode). “Weak” updrafts and downdrafts refer to those with a magnitude between 0 and 1 m s^{-1} , “moderate” between 1 and 5 m s^{-1} , “strong” from 5 to 10 m s^{-1} , and “very strong” greater than 10 m s^{-1} .

Differences from ls-100 run	Weak updrafts	Weak downdrafts	Moderate updrafts	Moderate downdrafts	Strong updrafts	Strong downdrafts	Very strong updrafts	Very strong downdrafts
hs-100								
Low levels	-0.61%	-2.58%	-20.8%	-33.4%	-24.7%	-59.3%	-2.63%	-100%
Midlevels	-14.9%	-16.0%	-53.6%	-38.9%	-60.6%	-67.7%	-59.1%	-75.0%
Upper levels	-45.3%	-46.2%	-95.4%	-98.0%	-98.0%	-98.1%	-97.1%	-100%
hs-500								
Low levels	+7.43%	-0.03%	-22.0%	+46.4%	-20.6%	+49.5%	+13.7%	0%
Midlevels	-9.57%	-13.5%	-57.5%	-24.8%	-67.4%	-40.0%	-62.2%	-35.0%
Upper levels	-44.9%	-45.9%	-97.4%	-95.2%	-97.3%	-92.2%	-86.7%	-100%
hs-3000								
Low levels	+11.7%	-1.61%	-25.4%	+307%	-23.2%	+2450%	+26.6%	+95.5%
Midlevels	+26.8%	+14.5%	-46.7%	+59.8%	-76.1%	+766%	-69.1%	+50.0%
Upper levels	-44.6%	-46.0%	-99.6%	-98.9%	-99.8%	-99.4%	-99.9%	-100%
ms-100								
Low levels	-0.02%	-0.61%	-1.52%	-7.07%	-7.44%	+19.5%	-7.34%	-75.0%
Midlevels	+2.81%	+3.88%	+8.77%	+1.77%	+6.43%	-11.2%	-20.0%	-16.7%
Upper levels	-3.99%	+6.28%	+25.0%	+44.7%	+17.7%	+35.8%	+31.2%	-19.2%
ms-500								
Low levels	+9.60%	+3.76%	+2.62%	+111%	+2.16%	+412%	+38.2%	+100%
Midlevels	+29.3%	+29.8%	+45.2%	+68.2%	+41.3%	+105%	+51.0%	+45.7%
Upper levels	+146%	+455%	+329%	+458%	+197%	+268%	+237%	+44.1%
ms-3000								
Low levels	+13.2%	+0.36%	-21.6%	+305%	-19.2%	+2480%	+5.95%	+107%
Midlevels	+34.6%	+21.6%	-41.6%	+70.5%	-73.1%	+723%	-71.9%	+21.4%
Upper levels	-42.9%	-44.1%	-99.3%	-97.9%	-99.6%	-99.3%	-99.8%	-100%
ls-500								
Low levels	+10.3%	+5.04%	+17.8%	+116%	+10.8%	+155%	+51.7%	-100%
Midlevels	+30.2	+31.7%	+55.6%	+79.4%	+46.3%	+92.8%	+46.5%	+33.3%
Upper levels	+47.0%	+142%	+122%	+272%	+38.9%	+152%	+94.7%	+5.56%
ls-3000								
Low levels	+14.7%	+2.23%	-17.6%	+322%	-13.0%	+2540%	+16.7%	+103%
Midlevels	+39.3%	+26.9%	-36.3%	+80.2%	-66.8%	+709%	-56.8%	+29.4%
Upper levels	-42.2%	-43.5%	-98.7%	-95.7%	-99.1%	-96.3%	-98.7%	-100%

the bulk environment, cloud and precipitation processes themselves, and radiative transfer.

b. The response of cloud mode properties to static stability and aerosol

Cloud mode characteristics were obtained by saving all grid points classified as a particular convective mode at all analysis times, and then calculating statistics, mean profiles, and net profiles over all the times when at least one cloud of a particular mode (categorized as discussed in section 2b) was present. The cloud properties in Figs. 11–14 are separated by mode, with the top row showing the control (ls-100) profiles for

cumulus (Figs. 11a, 12a, 13a, 14a), congestus (Figs. 11b, 12b, 13b, 14b), and cumulonimbus (Figs. 11c, 12c, 13c, 14c), and the bottom row (Figs. 11d–f, 12d–f, 13d–f, 14d–f) showing the simulation differences from the control for each mode, respectively. Note that each column’s vertical axis differs—cumulus extend to 4 km, congestus to 7 km, and cumulonimbus to about 14 km—and also recall the presence of background stable layers at ~ 1 km (boundary layer), ~ 6.5 km (freezing level), and ~ 16 km (tropopause).

Cumulus clouds are small, dynamically weak, and numerous in the ls-100 simulation (Table 4). The average cumulus cloud precipitates weakly, if at all, resulting in a low condensate mixing ratio below 500 m in the mean and a sharp

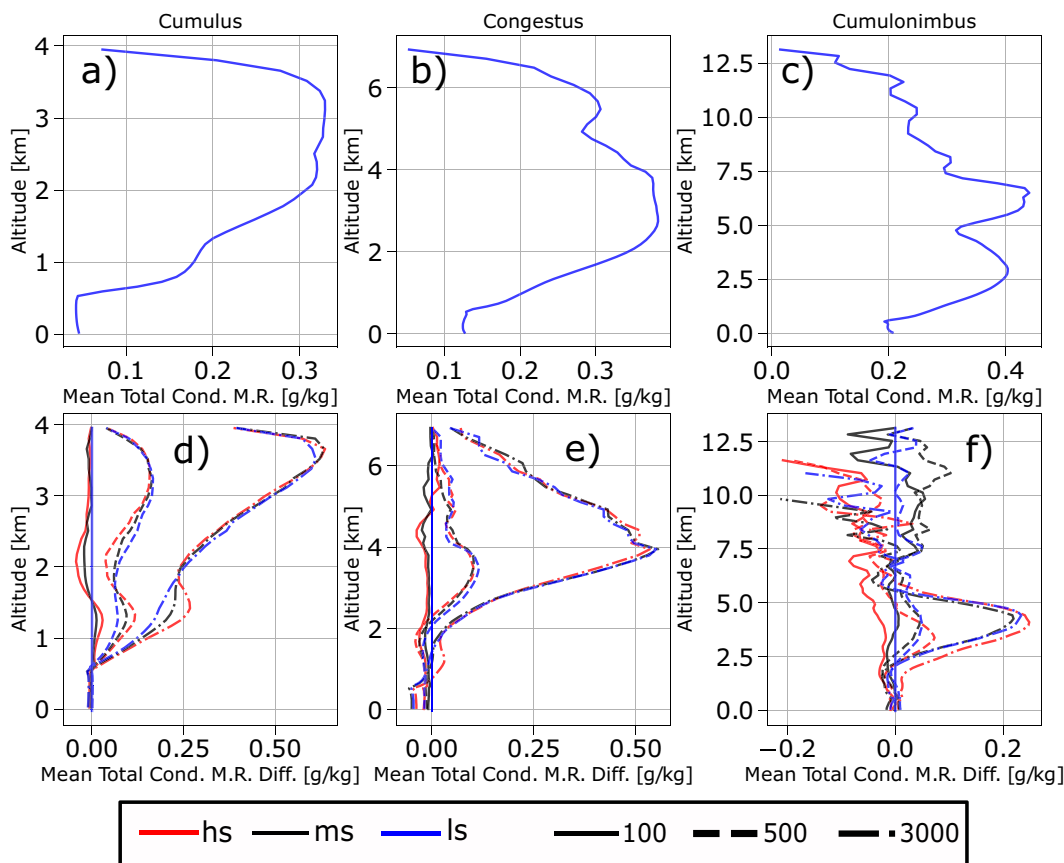


FIG. 11. Profiles of mean total condensate mixing ratio (“total cond. M. R.”) for the (a) cumulus, (b) congestus, and (c) cumulonimbus modes for the ls-100 control simulation, and differences from control for the other sensitivity experiments for the (d) cumulus, (e) congestus, and (f) cumulonimbus modes. Note that each column’s vertical axis differs—(left) cumulus extend to 4 km, (center) congestus to 7 km, and (right) cumulonimbus to about 14 km.

increase above this height (Fig. 11a). Cumulus deeper than the mean CTH exhibit heavier condensate loading between 2 and 3.5 km that then drops off sharply just below the 4 km cutoff. The mean vertical mass flux is negative below 500 m indicating precipitation and/or sedimentation, is positive from 500 to 1500 m, and increasingly negative above 1500 m (Fig. 12a). When aggregated to consider the net vertical mass transport by the cumulus mode, there is a strongly positive net flux between 500 and 1500 m, with considerably weaker negative fluxes above and below this level (Fig. 13a), indicating that cumulus primarily act to transport mass, moisture, and heat upward within the boundary layer, as noted in previous studies (e.g., Johnson et al. 1999; Schumacher et al. 2004). The mean moist static energy (MSE) contained within the cumulus mode is highest at the surface, with an additional local maximum just above 500 m (Fig. 14a). The mean MSE decreases sharply from 500 to about 1200 m, where environmental static stability is the lowest and entrainment may reduce MSE. Above 1200 m, this reduction is slower and more even.

When stability is increased for the same aerosol loading, the CTH and mean maximum vertical velocity of cumulus clouds are unambiguously suppressed (Table 4). However,

stability-driven changes in mean maximum area and frequency are modulated by aerosol loading. With greater static stability, condensate loading (Fig. 11d) and MSE (Fig. 14d) are enhanced in the boundary layer and reduced above, while the opposite trends are seen in the vertical mass fluxes (Figs. 12 and 13d). Enhanced low-level static stability reduces the ability of cumulus to penetrate beyond the trade wind stable layer, which increases condensate loading and moisture within the boundary layer. This reinforces our discussion in section 3a regarding the impact of the strength of the trade wind stable layer on vertical cloud growth.

Increasing aerosol loading reduces the CTH, maximum vertical velocity, and maximum area of the cumulus mode (Table 4), in agreement with some previous studies (Xue et al. 2008). Despite this, there are some signs of warm-phase enhancement: greater condensate loading (Fig. 11d) that agrees with the second AIE (Albrecht 1989), greater MSE (Fig. 14d), and deeper positive mean mass flux (Fig. 12d). However, negative mean mass flux values higher in the column are enhanced for increased aerosol concentrations, and there is also reduced net vertical mass flux in parts of the boundary layer (Fig. 13d). Increasing condensate loading to the point of weighing down cumulus updrafts, as well as an enhancement of stability and

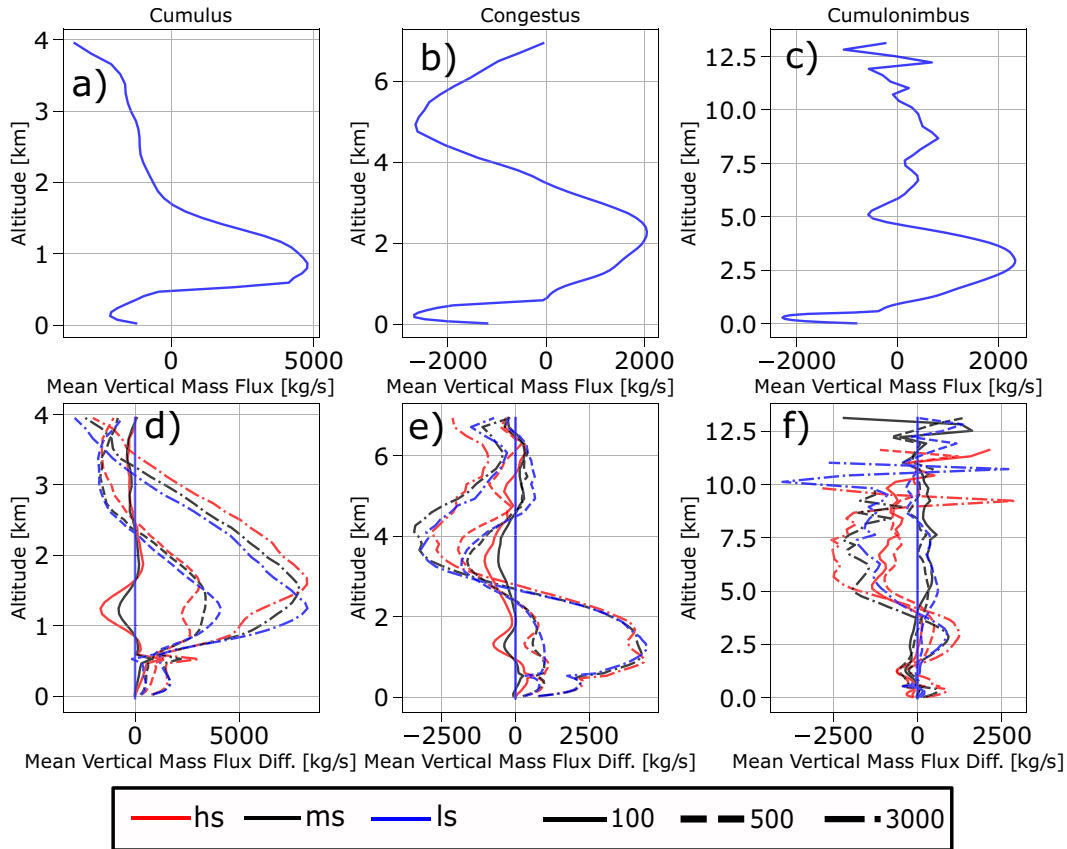


FIG. 12. Profiles of mean vertical mass flux. Each panel of the plot represents the same simulation(s) and cloud species as its counterpart in Fig. 11.

stratification above the boundary layer, contribute to these aerosol responses.

While the middle mode of congestus is about two orders of magnitude less frequent than the cumulus mode in our simulations, these clouds are much wider, taller, and more dynamically vigorous clouds. Their key statistics are presented in Table 5. Observational studies on tropical oceanic congestus are limited and definitions vary, so contextualizing these values is challenging—for example, previously defined CTH varies from as wide as 3–9 km (e.g., Luo et al. 2009) to as narrow as 5–7 km (e.g., Jensen and Del Genio 2006). Our values fit reasonably well within those reported by previous observational studies, albeit on the shallower and narrower side (e.g., Masunaga et al. 2005; Luo et al. 2009; Wall et al. 2013). Congestus clouds have greater condensate relative to cumulus, particularly in the lowest 500 m due to precipitating more frequently and heavily (Fig. 11b). A local maximum in condensate occurs between 2.5 and 4 km from warm and cold rain production, while another local maximum at 5.5 km (0.5–1 km above the freezing level) indicates boosts from ice production and lofted cloud water. Both maxima exhibit contributions from ice and cold rain production in transient congestus, which remain buoyant at the freezing level and continue growing (Luo et al. 2009; Leung and van den Heever 2022). The local minimum at 4.5–5 km is indicative of lower

condensate loading near cloud top in terminal congestus (also identified by Luo et al.), which are negatively buoyant at the freezing level, as well as enhanced freezing level detrainment (Zuidema 1998; Posselt et al. 2008). Some of these changes are reflected in the mean vertical mass flux profile, such as a stronger negative mean flux below 500 m (Fig. 12b). The region of positive mean flux is deeper than the cumulus mode (extending from ~500 to 3500 m), though its maximum value is about half as large, and the minimum around 4.75 km (near the freezing level) is roughly the maximum altitude terminal congestus would reach. The net vertical mass flux reflects similar patterns to the mean flux, further illuminating that most of the congestus mass transport occurs below ~3.5 km (Fig. 13b). However, the congestus net flux is about an order of magnitude less than for the cumulus mode, meaning that far less moisture is lofted to the midlevels via congestus than occurs within the lower levels due to cumulus transport. Finally, the congestus mean MSE profile in the low levels appears similar to that of cumulus but has a minimum around 4.5 km indicative of terminal congestus and an increase above this altitude from glaciation-related boosts to MSE from transient congestus (Fig. 14b).

Congestus exhibits two distinct behavioral regimes due to its more varied dependencies on the environment, which makes isolating individual responses to aerosol or static

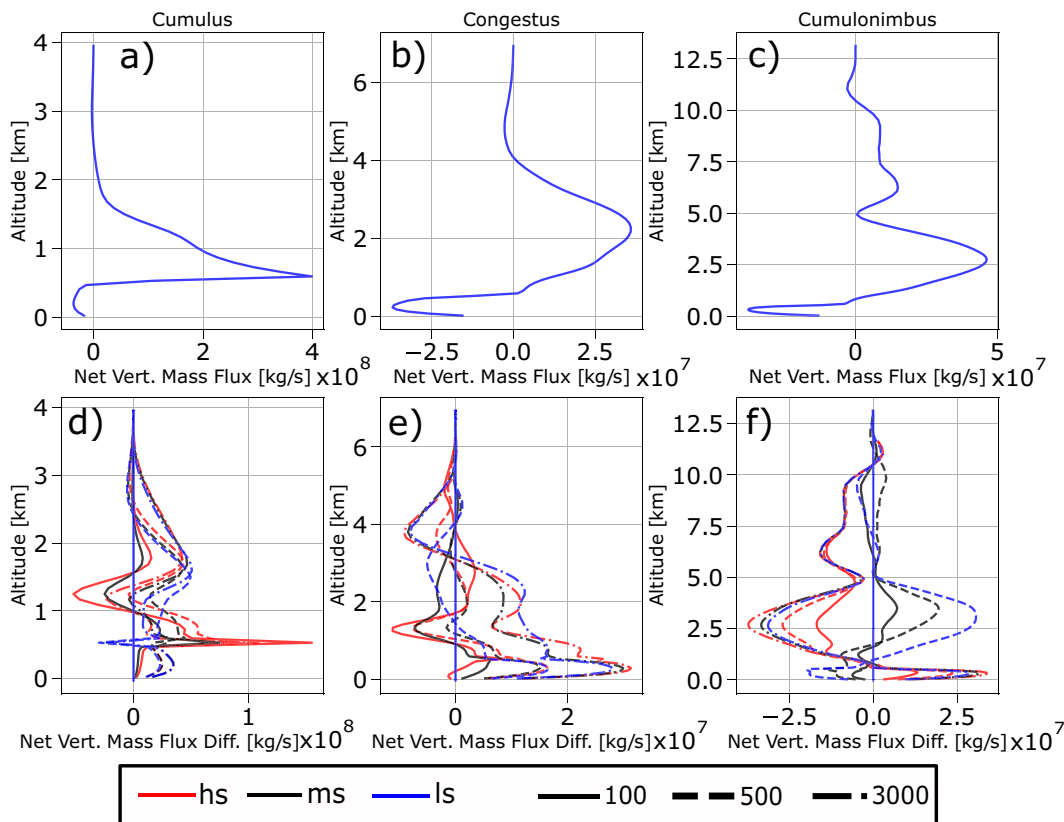


FIG. 13. Profiles of net vertical mass flux. Each panel of the plot represents the same simulation(s) and cloud species as its counterpart in Figs. 11 and 12. Note that the x -axis units for (a) and (d) are in $1 \times 10^{-8} \text{ kg s}^{-1}$, while the remainder are in $1 \times 10^7 \text{ kg s}^{-1}$.

stability more challenging. To first order, greater static stability results in narrower and more frequent congestus, but neither maximum vertical velocity nor CTH respond monotonically (Table 5). Stability impacts above the boundary layer are primarily modulated by aerosol, but higher stability also results in reduced precipitation. This can be seen through lower total condensate (Fig. 11e) and less-negative vertical mass fluxes (Figs. 12e and 13e) below 500 m, which subsequently increase congestus MSE within the boundary layer (Fig. 14e). On the other hand, first-order results from increasing aerosol concentrations are congestus that are shallower and narrower, but also more frequent in occurrence and dynamically vigorous (Table 5). Like enhanced stability, greater aerosol loading reduces precipitation (Figs. 11–13e). However, condensate loading is enhanced above 500 m and the mean vertical mass flux (Fig. 12e) is boosted below the freezing level with greater aerosol loading, both of which indicate warm-phase invigoration as identified by previous studies (e.g., Li et al. 2013; Sheffield et al. 2015).

Above the freezing level, some of the synergies discussed regarding the “Goldilocks zone” in section 3a manifest in congestus. While high aerosol loading substantially reduces mass fluxes above 4 km (Figs. 12e and 13e), moderate aerosol loading coupled with low-to-moderate boundary layer static stability appears to be the most favorable environment for more expansive and vigorous congestus. The increased stability acts

to enhance boundary layer moisture and energy. Coupled with the warm-phase invigoration from moderate aerosol loading, this allows developing congestus to draw on the enhanced MSE enough to invigorate its updraft and boost condensate loading, without too much condensate loading, entrainment, and evaporation weakening the updrafts.

Cumulonimbus are highly infrequent compared with the cumulus and congestus modes (Table 6), and only manifest once sufficient environmental moistening by cumulus and congestus has occurred. Tropical oceanic deep convection can reach the tropical tropopause in nature (Johnson et al. 1999), though our cumulonimbi are considerably shallower (Table 6) due to the high environmental wind shear (Igel and van den Heever 2015) and sharp drop in moisture above 10 km, in keeping with observations. The mean maximum vertical velocity also agrees well with that reported by Heymsfield et al. (2010). Cumulonimbus precipitate heavily, exhibiting much greater mean condensate loading in the lowest 500 m than either cumulus or congestus, as well as greater mean condensate loading overall (Fig. 11c). The condensate loading profile also reveals greater maxima above and below the freezing level than congestus, indicating greater ice and cold rain production, and a less-prominent freezing level local minimum that is typically associated with greater freezing level stability and detrainment (e.g., Posselt et al. 2008). The mean vertical

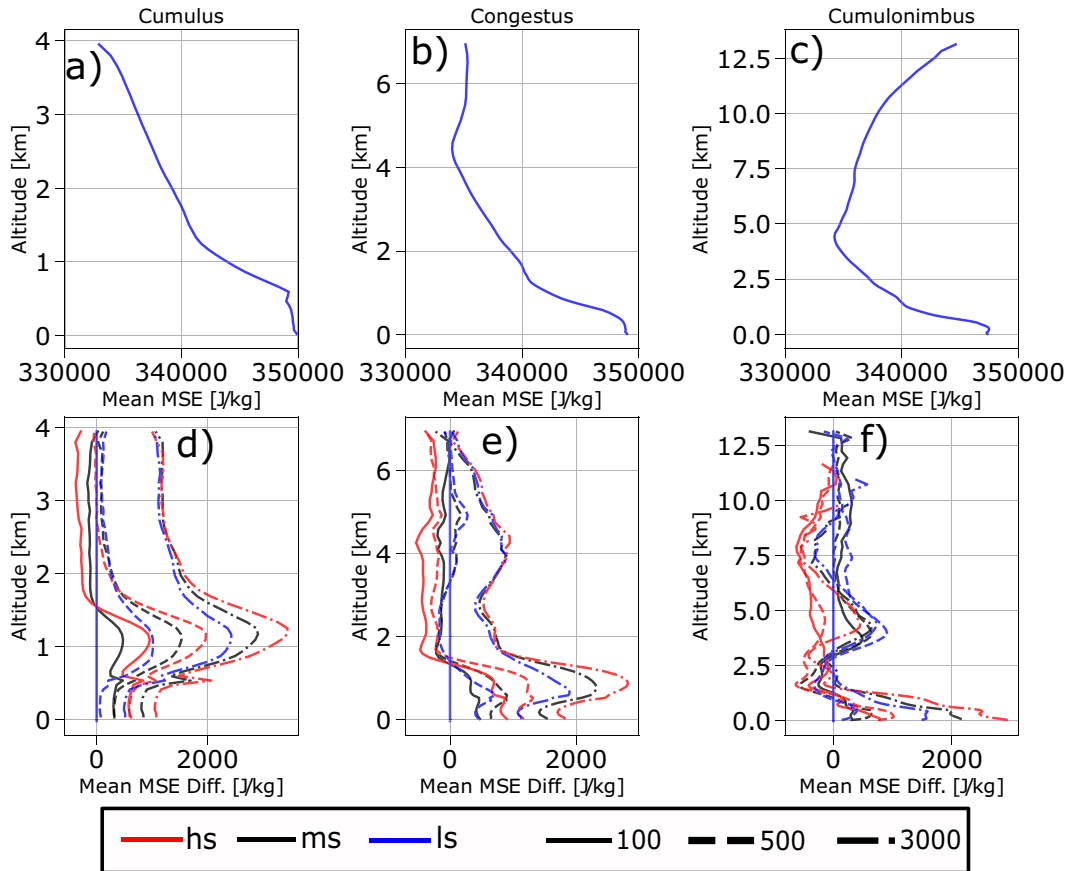


FIG. 14. Profiles of mean MSE. Each panel of the plot represents the same simulation(s) and cloud species as its counterpart in Figs. 11–13.

mass flux of the cumulonimbus mode has deeper positive transport ($\sim 1\text{--}4.5$ km) and weaker near-surface and freezing level negative mean fluxes than the congestus mode, as well as positive mean flux from ~ 6 to 10 km (Fig. 12c). The net vertical mass flux is of the same magnitude as that for congestus but produces greater positive net flux in the low levels, and a positive net flux from ~ 1 km through the freezing level all the way up to ~ 10 km (Fig. 13c), exhibiting deep mass,

moisture, and heat transport past the freezing level by cumulonimbus as characterized by Schumacher et al. (2004). Last, the mean MSE profile for cumulonimbus largely mirrors that of cumulus and congestus for the lower levels but increases more steadily above 4.5 km (except for a relatively static layer around 7 km) and reaches a maximum nearing that of the surface value at the top of the profile (Fig. 14c), further indicating deep transport of near-surface MSE.

TABLE 4. Some key characteristics [cloud-top height (m), maximum vertical velocity (w max; m s^{-1}), maximum areal coverage (km^2), single-time step mean count, and total count] of clouds which were classified as cumulus in each simulation. For each pair of values, the leftmost number is the arithmetic mean, and the rightmost number following the \pm is the standard deviation. All clouds identified as cumulus between 0200 UTC 21 Aug (2 h after initialization) and 0000 UTC 23 Aug were included in this analysis.

Simulation	CTH (m)	w max (m s^{-1})	Max area (km^2)	Mean count	Total count
hs-100	958.01 \pm 541.41	1.574 \pm 1.917	0.1994 \pm 0.3006	6312.0 \pm 1559.4	3.49 $\times 10^6$
hs-500	941.36 \pm 522.02	1.497 \pm 1.918	0.1662 \pm 0.2399	6591.3 \pm 1215.9	3.64 $\times 10^6$
hs-3000	871.55 \pm 456.46	1.329 \pm 1.811	0.1497 \pm 0.1840	6227.3 \pm 899.54	3.44 $\times 10^6$
ms-100	964.84 \pm 542.02	1.576 \pm 1.951	0.2002 \pm 0.3151	6027.2 \pm 1559.7	3.33 $\times 10^6$
ms-500	952.25 \pm 524.32	1.502 \pm 1.944	0.1637 \pm 0.2401	6414.7 \pm 1376.4	3.55 $\times 10^6$
ms-3000	895.68 \pm 471.90	1.364 \pm 1.851	0.1458 \pm 0.1763	6435.7 \pm 826.93	3.56 $\times 10^6$
ls-100	971.20 \pm 541.78	1.579 \pm 1.988	0.2024 \pm 0.3393	5703.0 \pm 1558.6	3.15 $\times 10^6$
ls-500	971.22 \pm 540.38	1.522 \pm 1.989	0.1637 \pm 0.2489	6211.7 \pm 1542.7	3.44 $\times 10^6$
ls-3000	916.71 \pm 485.94	1.385 \pm 1.885	0.1425 \pm 0.1758	6464.6 \pm 919.73	3.57 $\times 10^6$

TABLE 5. As in Table 4, but for those clouds classified as congestus.

Simulation	CTH (m)	w max (m s^{-1})	Max area (km^2)	Mean count	Total count
hs-100	4802.9 ± 739.00	11.48 ± 4.123	6.517 ± 6.772	32.991 ± 33.280	1.13×10^4
hs-500	4758.3 ± 699.08	12.02 ± 4.039	5.225 ± 4.937	32.689 ± 35.680	1.26×10^4
hs-3000	4730.7 ± 637.77	13.12 ± 4.090	4.044 ± 4.017	29.331 ± 26.945	1.10×10^4
ms-100	4800.4 ± 730.22	11.49 ± 4.025	7.109 ± 7.754	25.763 ± 21.014	9.22×10^3
ms-500	4826.8 ± 758.73	12.23 ± 4.051	6.286 ± 6.645	26.057 ± 25.105	9.64×10^3
ms-3000	4720.8 ± 633.72	12.89 ± 4.035	4.120 ± 4.557	28.647 ± 28.587	1.10×10^4
ls-100	4795.2 ± 717.68	11.58 ± 4.050	7.892 ± 9.145	25.401 ± 14.704	9.20×10^3
ls-500	4783.2 ± 747.98	12.10 ± 4.037	6.323 ± 7.141	22.461 ± 21.241	8.33×10^3
ls-3000	4736.1 ± 652.03	12.86 ± 4.036	4.387 ± 4.810	29.825 ± 28.118	1.09×10^4

The cumulonimbus mode responses to perturbations of initial stability and aerosols are even more complex and nonlinear than congestus. Cumulonimbi tend to be shallower and smaller in area but more dynamically intense at high static stability and are most frequent at midlevel static stability (Table 6). Signs of precipitation suppression, such as low-level mass flux changes (Figs. 12f and 13f), are not robust despite reduced condensate loading (Fig. 11f) and enhanced boundary layer moisture (seen through MSE changes, Fig. 14f). This illustrates the greater role of cold-phase precipitation in cumulonimbus versus cumulus and congestus, and the relative insensitivity of such processes to boundary layer static stability alone, despite the latter's role in the evolution of boundary layer moisture and energy. Indeed, a regime separation can be seen between the ms-100, ms-500, and ls-500 responses and those of the other runs, particularly above 4 km, further highlighting the nonlinearity present.

Regarding aerosols, moderate loading produces the deepest, strongest, and most frequent cumulonimbus, though the greatest cloud area is seen at low aerosol loadings (Table 6). With enhanced aerosol concentrations, condensate loading (Fig. 11f), mean vertical mass flux (Fig. 12f), and mean MSE (Fig. 14f) are generally enhanced from 2 to 6 km, 2 to 4 km, and 3 to 6 km, respectively, all of which are strong signs of warm-phase invigoration. Values above these altitudes, however, are reduced at high aerosol loading and otherwise modulated by stability, and the net vertical mass flux (Fig. 13f) shows a strong regime separation above 2 km. Boundary layer MSE is consistently enhanced with greater aerosol (Fig. 14f), but not above the freezing level due to the mixed cold-phase responses. Considered as a whole, these responses illustrate similar ‘‘Goldilocks zone’’ sensitivities for cumulonimbus as we

noted for congestus: the control (ls-100) environment is favorable for deep convection, and moderate increases to aerosol (ls-500, ms-500) or static stability (ms-100, ms-500) preserve or enhance convective ingredients present in ls-100 by providing more vapor growth sites, enhanced condensate lofting (aerosol); increased boundary layer moisture and energy (stability); or some combination of these. These findings agree with several studies in the literature (e.g., Khain et al. 2005, 2008; Fan et al. 2009; Storer et al. 2010, 2014; Marinescu et al. 2021; Park and van den Heever 2022) that identify mitigating environmental factors on robust warm and cold-phase invigoration from increased aerosol loading.

In summary, each of the three cloud modes evident in these simulations exhibit characteristics that are generally consistent with observations (e.g., Johnson et al. 1999) and the understood role that each mode plays in vertical mass, heat, and moisture transport (e.g., Schumacher et al. 2004). Their changes in response to perturbations in initial static stability and aerosol profiles are also in keeping with past literature. However, the complex modulations and interactions between different aspects of the responses to aerosol loading and static stability indicate the importance of considering mitigating factors and environmental characteristics when assessing aerosol–cloud interactions.

4. Conclusions and future work

Our primary research goal was to explore the sensitivities of the tropical trimodal convective distribution, convective environment, and upscale growth of convection to changes in static stability and aerosol loading. We considered the impacts of covarying three different initial static stabilities and three different initial aerosol profiles in a base environment representative

TABLE 6. As in Tables 4 and 5, but for those clouds classified as cumulonimbus.

Simulation	CTH (m)	w max (m s^{-1})	Max area (km^2)	Mean count	Total count
hs-100	7795.2 ± 853.65	16.65 ± 5.482	39.29 ± 36.91	3.9909 ± 2.6302	4.39×10^2
hs-500	7875.9 ± 921.86	16.89 ± 5.255	28.23 ± 22.19	3.0667 ± 1.8633	3.22×10^2
hs-3000	7626.7 ± 560.35	17.75 ± 4.941	16.71 ± 8.296	1.8690 ± 1.0210	1.57×10^2
ms-100	8719.8 ± 1636.1	16.62 ± 5.725	76.21 ± 66.37	4.2550 ± 2.3606	6.34×10^2
ms-500	8582.2 ± 1504.2	17.12 ± 5.742	62.41 ± 76.11	6.2797 ± 3.6992	8.98×10^2
ms-3000	7709.2 ± 613.97	16.54 ± 4.601	22.74 ± 13.75	1.9208 ± 1.1997	1.94×10^2
ls-100	8670.2 ± 1610.2	16.45 ± 6.657	76.80 ± 71.32	3.8675 ± 2.1887	5.84×10^2
ls-500	8806.7 ± 1513.2	17.47 ± 6.194	70.03 ± 70.08	5.6225 ± 3.2013	8.49×10^2
ls-3000	7759.6 ± 661.64	17.16 ± 4.670	22.67 ± 13.80	2.3047 ± 1.3951	2.95×10^2

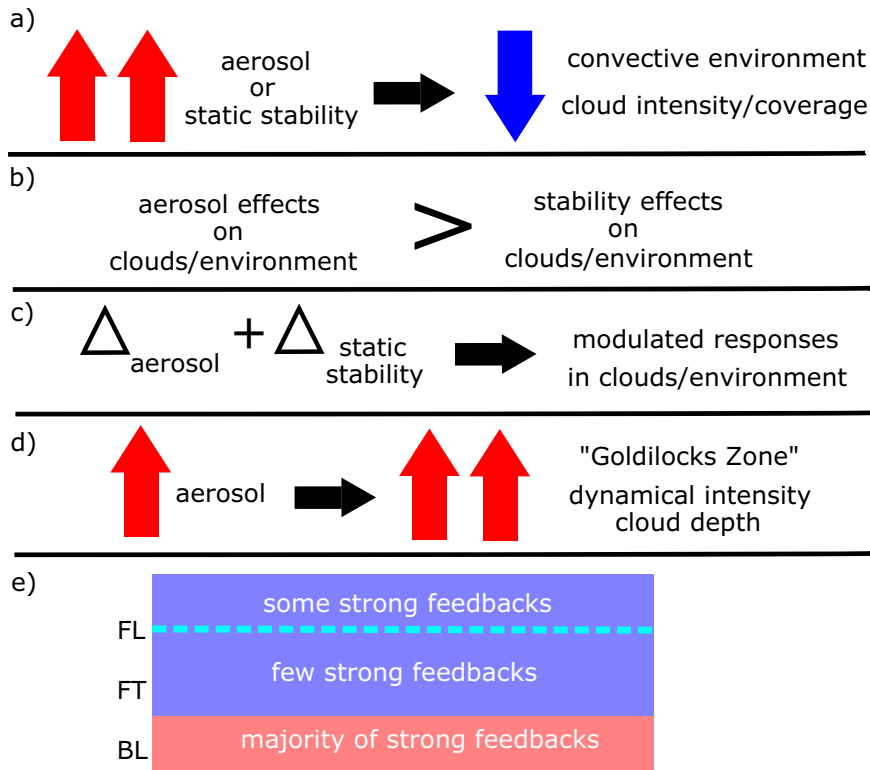


FIG. 15. A schematic of the five key conclusions drawn from this study. These include (a) the suppression of the bulk environment and the trimodal convective distribution from high amounts of aerosol loading and boundary layer static stability; (b) the dominance of aerosol effects over stability effects on both clouds and environment; (c) the modulation of cloud/environment responses to static stability and aerosols by changing the characteristics of both; (d) the presence of a “Goldilocks zone” in dynamical strength and cloud depth of convective clouds due to moderate aerosol loading; and (e) the occurrence of most of the strong feedbacks in the boundary layer, with some strong feedbacks seen above the freezing level but relatively few within the warm-phase free troposphere. Double upward arrows indicate high levels of the noted quantity [i.e., high stability and/or high aerosol for (a)], the deltas in (c) denote changes to the subscripted initial characteristic, the single upward arrow in (d) denotes a moderate level of aerosol, and in (e), FL, FT, and BL represent the freezing level, free troposphere, and boundary layer, respectively.

of tropical maritime regions around the Philippines which were observed during CAMP²Ex. To this end, nine different simulations were run for 48 h of integration time using the RAMS model in an LES framework. Our analysis has shown that enhanced static stability and aerosol loading both substantially impact the evolution of a tropical, maritime environment and the associated cloud fields around the Philippines. This work has allowed us to draw five key conclusions as summarized in Fig. 15 and discussed as follows.

a. Large amounts of aerosol loading and low-level static stability suppress the bulk environment and the intensity and coverage of convective clouds (Fig. 15a)

Strong static stability traps more moisture and MSE in the boundary layer but is also a substantial barrier to penetration by convective updrafts. This can be seen in the environmental characteristics (Figs. 4–10) and cloud mode statistics (Tables 4–6). Changes to LW radiation from increased low-level

stability reinforce the initial perturbation structure and render the bulk environment far less dynamically (Fig. 9, Table 3) and convectively (Fig. 8, Tables 4–6) active versus lower-stability environments. Similarly, high aerosol loading produces warm-phase invigoration (Fig. 9) and increased condensate loading (Fig. 11), but the latter counteracts buoyancy enhancements from greater condensational heating and increased LW absorption by aerosols (Figs. 6 and 7) further enhances environmental stability stratification (Fig. 4). It appears that entraining cloud edges may have greater evaporative cooling owing to smaller (and subsequently easier-to-evaporate) drops than at lower aerosol loading, which is reinforced by the narrower clouds seen at high aerosol loading (Tables 4–6).

b. Cloud and environmental responses to aerosol loading tend to be stronger than those from static stability (Fig. 15b)

The right columns of Figs. 4–10 illustrate the dominance of high aerosol loading over the benefits of starting with a more

convectively favorable (i.e., lower-static-stability) environment. Beyond the impacts already discussed in the first bullet, the LW and total radiation evolution (Figs. 6 and 7, right columns) are stratified at high aerosol loading due to the vertical redistribution of aerosols. This causes a more stratified static stability structure, resulting in stronger boundary layer and freezing level stable layers that inhibit vertical development of deeper convection.

c. The effects of aerosol and stability perturbations modulate each other substantially (Fig. 15c)

This conclusion is best seen through the cloud mode statistics (Tables 4–6) and vertical profiles of condensate loading, mean and net vertical mass flux, and MSE (Figs. 11–14, respectively). The shallow cumulus mode shows a weak modulation of effects versus deeper convection, with robust trends in the cloud mode statistics (Table 4) and stability mostly altering the dominant effects of aerosol as a function of height in the vertical profiles (Figs. 11d–14d). However, congestus and cumulonimbus (Tables 5 and 6) exhibit less monotonic trends with stability and aerosol, indicating greater nonlinearity in the combined effects of perturbed stability and aerosol. This is more apparent above the freezing level, where profiles of congestus and especially cumulonimbus group into two primary regimes (Figs. 11–14e,f).

d. The deepest convection and highest dynamical intensity occur at moderate aerosol loading, rather than at low or high loading (Fig. 15d)

The “Goldilocks zone” runs of ms-100, ms-500, and ls-500 exhibit a more constructive stability-aerosol modulation of each property’s impacts on condensate loading (Figs. 11d,e,h), mean and net vertical mass fluxes (Figs. 12 and 13d,e,h), and mean MSE (Figs. 14d,e,h) than the other runs, which exhibit consistently less condensate loading, more negative vertical mass fluxes, and less MSE than our control ls-100 run. Deep convection reaches higher maximum and mean CTH values at moderate aerosol loading (Figs. 8 and 10, center columns, Table 6), largely due to the enhanced ice processes and lofting of supercooled water seen in the ice ratios in Fig. 10. Updraft and downdraft strengths in the ms-500 and ls-500 runs (Figs. 9e,h) also exhibit strong signs of both warm- and cold-phase invigoration versus strictly the warm phase seen at high aerosol loading. The mean radiative transfer profiles (Fig. 14) also indicate that the mid aerosol runs do not experience the strong stratification and enhancement of static stability from ~2 to 5 km present at high aerosol loading that inhibit upscale convective growth.

e. Most of the strongest feedbacks due to aerosol and stability perturbations are seen in the boundary layer, though some are stronger above the freezing level (Fig. 15e)

While this may seem self-evident due to our experimental approach, the persistence of some of these impacts and their more indirect effects came as a surprise. For example, the stability perturbation structure remained remarkably steady throughout our simulations, since perturbing the temperature affected the LW forcing directly in a positive feedback loop (Figs. 6a–f).

Strong boundary layer responses can also be seen in cloud fraction (Fig. 8) and the cumulus mode statistics (Table 4). However, when considering upscale growth, some of these impacts are more prominent above the freezing level, such as the “Goldilocks zone” enhancement of vertical mass fluxes and condensate loading in congestus and cumulonimbus, changes to ice ratio above 5 km (Fig. 10), and changes to stability throughout the column from LW absorption by aerosols.

In summary, this study has not only revealed many complex sensitivities to both thermodynamics and aerosol loading but has also illuminated several paths for future work that we plan to explore. For example, although we have learned a great deal about the bulk responses of the different cloud modes to aerosol loading and static stability, the impacts of these environmental factors on the evolution of the full cloud life cycles was not examined. A follow-up study examining these impacts on cloud life cycle is presently underway. Another avenue of future work would be to thoroughly compare the individual clouds in our simulations with observations (e.g., dropsonde, cloud probe, radar, radiometer, and lidar data) from the CAMP²Ex field campaign and other appropriate campaigns. This would further characterize the multifaceted processes occurring in such environments.

Acknowledgments. The research contained in this manuscript was made possible by funding from NASA on the CAMP²Ex project through Grant 80NSSC18K0149, and the authors thank NASA for their support on this project. Hersbach et al. (2018) was downloaded from the Copernicus Climate Change Service (C3S) Climate Data Store. The results contain modified Copernicus Climate Change Service information 2021. Neither the European Commission nor ECMWF is responsible for any use that may be made of the Copernicus information or data it contains. We also thank Mr. Stephen M. Saleeby (Colorado State University) for his feedback on model configuration and nuances during this study, Dr. Jungmin “Minnie” Park (Brookhaven National Laboratory) for her thoughts on how to best condense some of the science within this manuscript, Dr. Jeffrey S. Reid (Naval Research Laboratory) for his input on environmental aerosol characterization, and Dr. Ralph E. Kuehn and Dr. Robert E. Holz (University of Wisconsin) for the use of Himawari satellite imagery from their NASA/University of Wisconsin GeoWorldview site (<http://geoworldview.ssec.wisc.edu>). Finally, we thank the three anonymous reviewers whose highly constructive comments helped to improve this manuscript.

Data availability statement. The source code of the RAMS version used (v. 6.2.12 with additional capability for parallel-compressed file writes) and all RAMS namelists needed to run the suite are included in the GitHub repository: https://github.com/galexsky/RAMS_LES_bulkpaper.git. The namelists used for each of the simulations are denoted “lsprism” for ls-100, “lsmid” for ls-500, “lspoll” for ls-3000, “ctrlprism” for ms-100, “ctrlmid” for ms-500, “ctrlpoll” for ms-3000, “hsprism” for hs-100, “hsmid” for hs-500, and “hspoll” for hs-3000.

REFERENCES

- Albrecht, B. A., 1989: Aerosols, cloud microphysics, and fractional cloudiness. *Science*, **245**, 1227–1230, <https://doi.org/10.1126/science.245.4923.1227>.
- Altartatz, O., I. Koren, Y. Yair, and C. Price, 2010: Lightning response to smoke from Amazonian fires. *Geophys. Res. Lett.*, **37**, L07801, <https://doi.org/10.1029/2010GL042679>.
- , —, L. A. Remer, and E. Hirsch, 2014: Review: Cloud invigoration by aerosols—Coupling between microphysics and dynamics. *Atmos. Res.*, **140–141**, 38–60, <https://doi.org/10.1016/j.atmosres.2014.01.009>.
- Andreae, M. O., D. Rosenfeld, P. Artaxo, A. A. Costa, G. P. Frank, K. M. Longo, and M. A. F. Silva-Dias, 2004: Smoking rain clouds over the Amazon. *Science*, **303**, 1337–1342, <https://doi.org/10.1126/science.1092779>.
- Arakawa, A., and V. R. Lamb, 1977: Computational design of the basic dynamical processes of the UCLA general circulation model. *Methods in Computational Physics: Advances in Research and Applications*, J. Chang, Ed., Vol. 17, Elsevier, 173–265.
- Atwood, S. A., and Coauthors, 2017: Size-resolved aerosol and cloud condensation nuclei (CCN) properties in the remote marine South China Sea— Part 1: Observations and source classification. *Atmos. Chem. Phys.*, **17**, 1105–1123, <https://doi.org/10.5194/acp-17-1105-2017>.
- Benedict, J. J., and D. A. Randall, 2007: Observed characteristics of the MJO relative to maximum rainfall. *J. Atmos. Sci.*, **64**, 2332–2354, <https://doi.org/10.1175/JAS3968.1>.
- Charlson, R. J., and M. J. Pilat, 1969: The influence of aerosols. *J. Appl. Meteor.*, **8**, 1001–1002, [https://doi.org/10.1175/1520-0450\(1969\)008<1001:CTIOA>2.0.CO;2](https://doi.org/10.1175/1520-0450(1969)008<1001:CTIOA>2.0.CO;2).
- Cotton, W. R., and Coauthors, 2003: RAMS 2001: Current status and future directions. *Meteor. Atmos. Phys.*, **82**, 5–29, <https://doi.org/10.1007/s00703-001-0584-9>.
- , G. H. Bryan, and S. C. van den Heever, 2011: *Storm and Cloud Dynamics*. Academic Press, 809 pp.
- Del Genio, A. D., and W. Kovari, 2002: Climatic properties of tropical precipitating convection under varying environmental conditions. *J. Climate*, **15**, 2597–2615, [https://doi.org/10.1175/1520-0442\(2002\)015<2597:CPOTPC>2.0.CO;2](https://doi.org/10.1175/1520-0442(2002)015<2597:CPOTPC>2.0.CO;2).
- , Y. Chen, D. Kim, and M.-S. Yao, 2012: The MJO transition from shallow to deep convection in *CloudSat/CALIPSO* data and GISS GCM simulations. *J. Climate*, **25**, 3755–3770, <https://doi.org/10.1175/JCLI-D-11-00384.1>.
- DeMott, P. J., and Coauthors, 2010: Predicting global atmospheric ice nuclei distributions and their impacts on climate. *Proc. Natl. Acad. Sci. USA*, **107**, 11217–11222, <https://doi.org/10.1073/pnas.0910818107>.
- Emanuel, K. A., 1994: *Atmospheric Convection*. Oxford University Press, 580 pp.
- Fan, J., and Coauthors, 2009: Dominant role by vertical wind shear in regulating aerosol effects on deep convective clouds. *J. Geophys. Res.*, **114**, D22206, <https://doi.org/10.1029/2009JD012352>.
- Feingold, G., B. Stevens, W. R. Cotton, and A. S. Frisch, 1996: The relationship between drop in-cloud residence time and drizzle production in numerically simulated stratus clouds. *J. Atmos. Sci.*, **53**, 1108–1122, [https://doi.org/10.1175/1520-0469\(1996\)053<1108:TRBDIC>2.0.CO;2](https://doi.org/10.1175/1520-0469(1996)053<1108:TRBDIC>2.0.CO;2).
- Freeman, S. W., S. C. van den Heever, J. S. Reid, and D. J. Posselt, 2019: Tropical deep convective morphology in the different thermodynamic and aerosol environments of CAMP²Ex and PISTON. *2019 Fall Meeting*, San Francisco, CA, Amer. Geophys. Union, Abstract A34A-05, <https://agu.confex.com/agu/fm19/meetingapp.cgi/Paper/552100>.
- Ghate, V. P., M. A. Miller, and P. Zhu, 2016: Differences between nonprecipitating tropical and trade wind marine shallow cumuli. *Mon. Wea. Rev.*, **144**, 681–701, <https://doi.org/10.1175/MWR-D-15-0110.1>.
- Grabowski, W. W., 2018: Can the impact of aerosols on deep convection be isolated from meteorological effects in atmospheric observations? *J. Atmos. Sci.*, **75**, 3347–3363, <https://doi.org/10.1175/JAS-D-18-0105.1>.
- , and H. Morrison, 2020: Do ultrafine cloud condensation nuclei invigorate deep convection? *J. Atmos. Sci.*, **77**, 2567–2583, <https://doi.org/10.1175/JAS-D-20-0012.1>.
- Harrington, J. Y., 1997: The effects of radiative and microphysical processes on simulated warm and transition season Arctic stratus. Ph.D. dissertation, Colorado State University, 278 pp.
- Harrop, B. E., and D. L. Hartmann, 2015: The relationship between atmospheric convective radiative effect and net energy transport in the tropical warm pool. *J. Climate*, **28**, 8620–8633, <https://doi.org/10.1175/JCLI-D-15-0151.1>.
- Hersbach, H., and Coauthors, 2018: ERA5 hourly data on pressure levels from 1979 to present. C3S CDS, accessed 19 November 2019, <https://doi.org/10.24381/cds.bd0915c6>.
- Heus, T., and A. Seifert, 2013: Automated tracking of shallow cumulus clouds in large domain, long duration large eddy simulations. *Geosci. Model Dev.*, **6**, 1261–1273, <https://doi.org/10.5194/gmd-6-1261-2013>.
- Heymsfield, G. M., L. Tian, A. J. Heymsfield, L. Li, and S. Guimond, 2010: Characteristics of deep tropical and subtropical convection from nadir-viewing high-altitude airborne Doppler radar. *J. Atmos. Sci.*, **67**, 285–308, <https://doi.org/10.1175/2009JAS3132.1>.
- Hilario, M. R. A., and Coauthors, 2020: Investigating size-segregated sources of elemental composition of particulate matter in the South China Sea during the 2011 Vasco cruise. *Atmos. Chem. Phys.*, **20**, 1255–1276, <https://doi.org/10.5194/acp-20-1255-2020>.
- Hohenegger, C., and B. Stevens, 2013: Preconditioning deep convection with cumulus congestus. *J. Atmos. Sci.*, **70**, 448–464, <https://doi.org/10.1175/JAS-D-12-089.1>.
- Igel, A. L., and S. C. van den Heever, 2021: Invigoration or enervation of convective clouds by aerosols? *Geophys. Res. Lett.*, **48**, e2021GL093804m, <https://doi.org/10.1029/2021GL093804>.
- Igel, M. R., and S. C. van den Heever, 2015: The relative influence of environmental characteristics on tropical deep convective morphology as observed by CloudSat. *J. Geophys. Res. Atmos.*, **120**, 4304–4322, <https://doi.org/10.1002/2014JD022690>.
- Jakob, C., G. Tselioudis, and T. Hume, 2005: The radiative, cloud, and thermodynamic properties of the major tropical western Pacific cloud regimes. *J. Climate*, **18**, 1203–1215, <https://doi.org/10.1175/JCLI3326.1>.
- Jensen, M. P., and A. D. Del Genio, 2006: Factors limiting convective cloud-top height at the ARM Nauru Island climate research facility. *J. Climate*, **19**, 2105–2117, <https://doi.org/10.1175/JCLI3722.1>.
- Johnson, R. H., T. M. Rickenbach, S. A. Rutledge, P. E. Ciesielski, and W. H. Schubert, 1999: Trimodal characteristics of tropical convection. *J. Climate*, **12**, 2397–2418, [https://doi.org/10.1175/1520-0442\(1999\)012<2397:TCOTC>2.0.CO;2](https://doi.org/10.1175/1520-0442(1999)012<2397:TCOTC>2.0.CO;2).
- Khain, A., D. Rosenfeld, and A. Pokrovsky, 2005: Aerosol impact on the dynamics and microphysics of deep convective clouds. *Quart. J. Roy. Meteor. Soc.*, **131**, 2639–2663, <https://doi.org/10.1256/qj.04.62>.

- , N. BenMoshe, and A. Pokrovsky, 2008: Factors determining the impact of aerosols on surface precipitation from clouds: An attempt at classification. *J. Atmos. Sci.*, **65**, 1721–1748, <https://doi.org/10.1175/2007JAS2515.1>.
- Lebo, Z. J., and J. H. Seinfeld, 2011: Theoretical basis for convective invigoration due to increased aerosol concentration. *Atmos. Chem. Phys.*, **11**, 5407–5429, <https://doi.org/10.5194/acp-11-5407-2011>.
- , H. Morrison, and J. H. Seinfeld, 2012: Are simulated aerosol-induced effects on deep convective clouds strongly dependent on saturation adjustment? *Atmos. Chem. Phys.*, **12**, 9941–9964, <https://doi.org/10.5194/acp-12-9941-2012>.
- Lee, T. J., 1992: The impact of vegetation on the atmospheric boundary layer and convective storms. Ph.D. dissertation, Colorado State University, 128 pp.
- Leung, G. R., and S. C. van den Heever, 2022: Controls on the development and circulation of terminal versus transient congestus clouds and implications for midlevel aerosol transport. *J. Atmos. Sci.*, <https://doi.org/10.1175/JAS-D-21-0314.1>, in press.
- Li, X., W.-K. Tao, H. Masunaga, G. Gu, and X. Zeng, 2013: Aerosol effects on cumulus congestus population over the tropical Pacific: A cloud-resolving modeling study. *J. Meteor. Soc. Japan*, **91**, 817–833, <https://doi.org/10.2151/jmsj.2013-607>.
- Liu, C., and M. W. Moncrieff, 1998: A numerical study of the diurnal cycle of tropical oceanic convection. *J. Atmos. Sci.*, **55**, 2329–2344, [https://doi.org/10.1175/1520-0469\(1998\)055<2329:ANSOTD>2.0.CO;2](https://doi.org/10.1175/1520-0469(1998)055<2329:ANSOTD>2.0.CO;2).
- Luo, Z., G. Y. Liu, G. L. Stephens, and R. H. Johnson, 2009: Terminal versus transient cumulus congestus: A CloudSat perspective. *Geophys. Res. Lett.*, **36**, L05808, <https://doi.org/10.1029/2008GL036927>.
- Malkus, J. S., 1958: On the structure of the trade wind moist layer. *Phys. Oceanogr. Meteor.*, **13**, 1–48, <https://doi.org/10.1575/1912/1065>.
- , and H. Riehl, 1964: Cloud structure and distributions over the tropical Pacific Ocean. *Tellus*, **16**, 275–287, <https://doi.org/10.3402/TELLUSA.V16I3.8980>.
- Marinescu, P. J., and Coauthors, 2021: Impacts of varying concentrations of cloud condensation nuclei on deep convective cloud updrafts—A multimodel assessment. *J. Atmos. Sci.*, **78**, 1147–1172, <https://doi.org/10.1175/JAS-D-20-0200.1>.
- Masunaga, H., T. S. L'Ecuyer, and C. D. Kummerow, 2005: Variability in the characteristics of precipitation systems in the tropical Pacific. Part I: Spatial structure. *J. Climate*, **18**, 823–840, <https://doi.org/10.1175/JCLI-3304.1>.
- Matsui, T., S. Q. Zhang, S. E. Lang, W.-K. Tao, C. Ichoku, and C. D. Peters-Lidard, 2018: Impact of radiation frequency, precipitation radiative forcing, and radiation column aggregation on convection-permitting West African monsoon simulations. *Climate Dyn.*, **55**, 193–213, <https://doi.org/10.1007/s00382-018-4187-2>.
- Maze, A., 1889: Sur la classification des nuages. *Congrès Météorologique International*, Congrès Météorologique International, 25–37.
- Meyers, M. P., R. L. Walko, J. Y. Harrington, and W. R. Cotton, 1997: New RAMS cloud microphysics parameterization. Part II: The two-moment scheme. *Atmos. Res.*, **45**, 3–39, [https://doi.org/10.1016/S0169-8095\(97\)00018-5](https://doi.org/10.1016/S0169-8095(97)00018-5).
- Neggens, R. A. J., J. D. Neelin, and B. Stevens, 2007: Impact mechanisms of shallow cumulus convection on tropical climate dynamics. *J. Climate*, **20**, 2623–2642, <https://doi.org/10.1175/JCLI4079.1>.
- Park, J. M., and S. C. van den Heever, 2022: Weakening of tropical sea breeze convective systems through interactions of aerosol, radiation, and soil moisture. *Atmos. Chem. Phys.*, **22**, 10 527–10 549, <https://doi.org/10.5194/acp-22-10527-2022>.
- Pielke, R. A., and Coauthors, 1992: A comprehensive meteorological modeling system—RAMS. *Meteor. Atmos. Phys.*, **49**, 69–91, <https://doi.org/10.1007/BF01025401>.
- Posselt, D. J., S. C. van den Heever, and G. L. Stephens, 2008: Trimodal cloudiness and tropical stable layers in simulations of radiative convective equilibrium. *Geophys. Res. Lett.*, **35**, L08802, <https://doi.org/10.1029/2007GL033029>.
- Randall, D. A., 1980: Conditional instability of the first kind up-side-down. *J. Atmos. Sci.*, **37**, 125–130, [https://doi.org/10.1175/1520-0469\(1980\)037<0125:CIOTFK>2.0.CO;2](https://doi.org/10.1175/1520-0469(1980)037<0125:CIOTFK>2.0.CO;2).
- Rauber, R. M., and Coauthors, 2007: Rain in shallow cumulus over the ocean: The RICO campaign. *Bull. Amer. Meteor. Soc.*, **88**, 1912–1928, <https://doi.org/10.1175/BAMS-88-12-1912>.
- Reid, J. S., and Coauthors, 2013: Observing and understanding the Southeast Asian aerosol system by remote sensing: An initial review and analysis for the Seven Southeast Asian Studies (7SEAS) program. *Atmos. Res.*, **122**, 403–468, <https://doi.org/10.1016/j.atmosres.2012.06.005>.
- , and Coauthors, 2016a: Aerosol meteorology of the Maritime Continent for the 2012 7SEAS southwest monsoon intensive study—Part 1: Regional-scale phenomena. *Atmos. Chem. Phys.*, **16**, 14 041–14 056, <https://doi.org/10.5194/acp-16-14041-2016>.
- , and Coauthors, 2016b: Aerosol meteorology of Maritime Continent for the 2012 7SEAS southwest monsoon intensive study—Part 2: Philippine receptor observations of fine-scale aerosol behavior. *Atmos. Chem. Phys.*, **16**, 14 057–14 078, <https://doi.org/10.5194/acp-16-14057-2016>.
- Riehl, H., and J. S. Malkus, 1958: On the heat balance of the equatorial trough zone. *Geophysica*, **6**, 503–538.
- Rosenfeld, D., and I. M. Lensky, 1998: Satellite-based insights into precipitation formation processes in continental and maritime convective clouds. *Bull. Amer. Meteor. Soc.*, **79**, 2457–2476, [https://doi.org/10.1175/1520-0477\(1998\)079<2457:SBIIPF>2.0.CO;2](https://doi.org/10.1175/1520-0477(1998)079<2457:SBIIPF>2.0.CO;2).
- , U. Lohmann, G. B. Raga, C. D. O'Dowd, M. Kulmala, S. Fuzzi, A. Reissell, and M. O. Andreae, 2008: Flood or drought: How do aerosols affect precipitation? *Science*, **321**, 1309–1313, <https://doi.org/10.1126/science.1160606>.
- Ruppert, J. H., Jr., and R. H. Johnson, 2015: Diurnally modulated cumulus moistening in the preonset stage of the Madden-Julian oscillation during DYNAMO. *J. Atmos. Sci.*, **72**, 1622–1647, <https://doi.org/10.1175/JAS-D-14-0218.1>.
- Saleeby, S. M., and S. C. van den Heever, 2013: Developments in the CSU-RAMS aerosol model: Emissions, nucleation, regeneration, deposition, and radiation. *J. Appl. Meteor. Climatol.*, **52**, 2601–2622, <https://doi.org/10.1175/JAMC-D-12-0312.1>.
- , S. R. Herbener, S. C. van den Heever, and T. L'Ecuyer, 2015: Impacts of cloud droplet–nucleating aerosols on shallow tropical convection. *J. Atmos. Sci.*, **72**, 1369–1385, <https://doi.org/10.1175/JAS-D-14-0153.1>.
- Schubert, W. H., 1976: Experiments with Lilly's cloud-topped mixed layer model. *J. Atmos. Sci.*, **33**, 436–446, [https://doi.org/10.1175/1520-0469\(1976\)033<0436:EWLCTM>2.0.CO;2](https://doi.org/10.1175/1520-0469(1976)033<0436:EWLCTM>2.0.CO;2).
- Schumacher, C., R. A. Houze Jr., and I. Kraucunas, 2004: The tropical dynamical response to latent heating estimates derived from the TRMM Precipitation Radar. *J. Atmos. Sci.*, **61**, 1341–1358, [https://doi.org/10.1175/1520-0469\(2004\)061<1341:TTDRTL>2.0.CO;2](https://doi.org/10.1175/1520-0469(2004)061<1341:TTDRTL>2.0.CO;2).

- , M. H. Zhang, and P. E. Ciesielski, 2007: Heating structures of the TRMM field campaigns. *J. Atmos. Sci.*, **64**, 2593–2610, <https://doi.org/10.1175/JAS3938.1>.
- Sheffield, A. M., S. M. Saleeby, and S. C. van den Heever, 2015: Aerosol-induced mechanisms for cumulus congestus growth. *J. Geophys. Res. Atmos.*, **120**, 8941–8952, <https://doi.org/10.1002/2015JD023743>.
- Squires, P., 1958: The microstructure and colloidal stability of warm clouds. *Tellus*, **10**, 256–261, <https://doi.org/10.3402/tellusa.v10i2.9229>.
- , and S. Twomey, 1960: The relation between cloud droplet spectra and the spectrum of cloud nuclei. *Physics of Precipitation: Proceedings of the Cloud Physics Conference, Geophys. Monogr.*, Vol. 5, Amer. Geophys. Union, 211–219.
- Storer, R. L., S. C. van den Heever, and G. L. Stephens, 2010: Modeling aerosol impacts on convective storms in different environments. *J. Atmos. Sci.*, **67**, 3904–3915, <https://doi.org/10.1175/2010JAS3363.1>.
- , —, and T. S. L'Ecuyer, 2014: Observations of aerosol-induced convective invigoration in the tropical east Atlantic. *J. Geophys. Res. Atmos.*, **119**, 3963–3975, <https://doi.org/10.1002/2013JD020272>.
- Sui, C.-H., K.-M. Lau, Y. N. Takayabu, and D. A. Short, 1997: Diurnal variations in tropical oceanic cumulus convection during TOGA COARE. *J. Atmos. Sci.*, **54**, 639–655, [https://doi.org/10.1175/1520-0469\(1997\)054<0639:DVITOC>2.0.CO;2](https://doi.org/10.1175/1520-0469(1997)054<0639:DVITOC>2.0.CO;2).
- Tao, W.-K., J.-P. Chen, Z. Li, C. Wang, and C. Zhang, 2012: Impact of aerosols on convective clouds and precipitation. *Rev. Geophys.*, **50**, RG2001, <https://doi.org/10.1029/2011RG000369>.
- Toms, B. A., E. A. Barnes, E. D. Maloney, and S. C. Heever, 2020a: The global teleconnection signature of the Madden-Julian oscillation and its modulation by the quasi-biennial oscillation. *J. Geophys. Res. Atmos.*, **125**, e2020JD032653, <https://doi.org/10.1029/2020JD032653>.
- , S. C. van den Heever, E. M. Riley Dellaripa, S. M. Saleeby, and E. D. Maloney, 2020b: The boreal summer Madden-Julian oscillation and moist convective morphology over the Maritime Continent. *J. Atmos. Sci.*, **77**, 647–667, <https://doi.org/10.1175/JAS-D-19-0029.1>.
- Twomey, S., 1974: Pollution and the planetary albedo. *Atmos. Environ.*, **8**, 1251–1256, [https://doi.org/10.1016/0004-6981\(74\)90004-3](https://doi.org/10.1016/0004-6981(74)90004-3).
- , 1977: The influence of pollution on the shortwave albedo of clouds. *J. Atmos. Sci.*, **34**, 1149–1152, [https://doi.org/10.1175/1520-0469\(1977\)034<1149:TIOPOT>2.0.CO;2](https://doi.org/10.1175/1520-0469(1977)034<1149:TIOPOT>2.0.CO;2).
- , M. Piepgrass, and T. L. Wolfe, 1984: An assessment of the impact of pollution on global cloud albedo. *Tellus*, **36A**, 356–366, <https://doi.org/10.3402/tellusb.v36i5.14916>.
- van den Heever, S. C., G. G. Carrió, W. R. Cotton, P. J. DeMott, and A. J. Prenni, 2006: Impacts of nucleating aerosol on Florida storms. Part I: Mesoscale simulations. *J. Atmos. Sci.*, **63**, 1752–1775, <https://doi.org/10.1175/JAS3713.1>.
- , G. L. Stephens, and N. B. Wood, 2011: Aerosol indirect effects on tropical convection characteristics under conditions of radiative-convective equilibrium. *J. Atmos. Sci.*, **68**, 699–718, <https://doi.org/10.1175/2010JAS3603.1>.
- , S. M., Saleeby, L. D. Grant, A. L. Igel, and S. W. Freeman, 2021: RAMS model/RAMS: RAMS release version 6.3.01. Zenodo, <https://zenodo.org/record/5348024#.YoZB-6jMKUK>.
- Varble, A., 2018: Erroneous attribution of deep convective invigoration to aerosol concentration. *J. Atmos. Sci.*, **75**, 1351–1368, <https://doi.org/10.1175/JAS-D-17-0217.1>.
- Virtanen, P., and Coauthors, 2020: SciPy1.0: Fundamental algorithms for scientific computing in Python. *Nat. Methods*, **17**, 261–272, <https://doi.org/10.1038/s41592-019-0686-2>.
- Walko, R. L., and Coauthors, 2000: Coupled atmosphere-biophysics-hydrology models for environmental modeling. *J. Appl. Meteor.*, **39**, 931–944, [https://doi.org/10.1175/1520-0450\(2000\)039<0931:CABHMF>2.0.CO;2](https://doi.org/10.1175/1520-0450(2000)039<0931:CABHMF>2.0.CO;2).
- Wall, C., C. Liu, and E. Zipser, 2013: A climatology of tropical congestus using CloudSat. *J. Geophys. Res. Atmos.*, **118**, 6478–6492, <https://doi.org/10.1002/jgrd.50455>.
- Wang, Y., B. Geerts, and J. French, 2009: Dynamics of the cumulus cloud margin: An observational study. *J. Atmos. Sci.*, **66**, 3660–3677, <https://doi.org/10.1175/2009JAS3129.1>.
- Warner, J., and S. Twomey, 1967: The production of cloud nuclei by cane fires and the effect on cloud droplet concentration. *J. Atmos. Sci.*, **24**, 704–706, [https://doi.org/10.1175/1520-0469\(1967\)024<0704:TPOCNB>2.0.CO;2](https://doi.org/10.1175/1520-0469(1967)024<0704:TPOCNB>2.0.CO;2).
- Weaver, J. R., 1985: Centrosymmetric (cross-symmetric) matrices, their basic properties, eigenvalues, and eigenvectors. *Amer. Math. Mon.*, **92**, 711–717, <https://doi.org/10.1080/00029890.1985.11971719>.
- Webster, P. J., and R. Lukas, 1992: TOGA COARE: The Coupled Ocean-Atmosphere Response Experiment. *Bull. Amer. Meteor. Soc.*, **73**, 1377–1416, [https://doi.org/10.1175/1520-0477\(1992\)073<1377:TCTCOR>2.0.CO;2](https://doi.org/10.1175/1520-0477(1992)073<1377:TCTCOR>2.0.CO;2).
- Weller, R. A., and S. C. Anderson, 1996: Surface meteorology and air-sea fluxes in the western equatorial Pacific warm pool during the TOGA Coupled Ocean-Atmosphere Response Experiment. *J. Climate*, **9**, 1959–1990, [https://doi.org/10.1175/1520-0442\(1996\)009<1959:SMAASF>2.0.CO;2](https://doi.org/10.1175/1520-0442(1996)009<1959:SMAASF>2.0.CO;2).
- Wood, R., C. S. Bretherton, D. Leon, A. D. Clarke, P. Zuidema, G. Allen, and H. Coe, 2011: An aircraft case study of the spatial transition from closed to open mesoscale cellular convection over the southeast Pacific. *Atmos. Chem. Phys.*, **11**, 2341–2370, <https://doi.org/10.5194/acp-11-2341-2011>.
- Xue, H., G. Feingold, and B. Stevens, 2008: Aerosol effects on clouds, precipitation, and the organization of shallow cumulus convection. *J. Atmos. Sci.*, **65**, 392–406, <https://doi.org/10.1175/2007JAS2428.1>.
- Yanai, M., S. Esbensen, and J.-H. Chu, 1973: Determination of bulk properties of tropical cloud clusters from large-scale heat and moisture budgets. *J. Atmos. Sci.*, **30**, 611–627, [https://doi.org/10.1175/1520-0469\(1973\)030<0611:DOBPOT>2.0.CO;2](https://doi.org/10.1175/1520-0469(1973)030<0611:DOBPOT>2.0.CO;2).
- Yuter, S. E., and R. A. Houze Jr., 1995: Three-dimensional kinematic and microphysical evolution of Florida cumulonimbus. Part II: Frequency distributions of vertical velocity, reflectivity, and differential reflectivity. *Mon. Wea. Rev.*, **123**, 1941–1963, [https://doi.org/10.1175/1520-0493\(1995\)123<1941:TDKAME>2.0.CO;2](https://doi.org/10.1175/1520-0493(1995)123<1941:TDKAME>2.0.CO;2).
- Zipser, E. J., 2003: Cloud systems, hurricanes, and the Tropical Rainfall Measuring Mission (TRMM). *Some Views on "Hot Towers" after 50 Years of Tropical Field Programs and Two Years of TRMM Data*, Meteor. Monogr., No. 51, Amer. Meteor. Soc., 49–58.
- Zuidema, P., 1998: The 600–800-mb minimum in tropical cloudiness observed during TOGA COARE. *J. Atmos. Sci.*, **55**, 2220–2228, [https://doi.org/10.1175/1520-0469\(1998\)055<2220:TMMITC>2.0.CO;2](https://doi.org/10.1175/1520-0469(1998)055<2220:TMMITC>2.0.CO;2).